Advanced Composites and Hybrid Materials (2024) 7:163
https://doi.org/10.1007/s42114-024-00962-y

RESEARCH

High-performance magnetic artificial silk fibers produced by a scalable and eco-friendly production method

Gabriele Greco[1] · Benjamin Schmuck[1,2] · Lucia Del Bianco[3] · Federico Spizzo[3] · Luca Fambri[4] · Nicola Maria Pugno[5,6] · Sabino Veintemillas-Verdaguer[7] · Maria Puerto Morales[7] · Anna Rising[1,2]

Received: 8 April 2024 / Revised: 5 July 2024 / Accepted: 14 September 2024

Abstract

Flexible magnetic materials have great potential for biomedical and soft robotics applications, but they need to be mechanically robust. An extraordinary material from a mechanical point of view is spider silk. Recently, methods for producing artificial spider silk fibers in a scalable and all-aqueous-based process have been developed. If endowed with magnetic properties, such biomimetic artificial spider silk fibers would be excellent candidates for making magnetic actuators. In this study, we introduce magnetic artificial spider silk fibers, comprising magnetite nanoparticles coated with meso-2,3-dimercaptosuccinic acid. The composite fibers can be produced in large quantities, employing an environmentally friendly wet-spinning process. The nanoparticles were found to be uniformly dispersed in the protein matrix even at high concentrations (up to 20% w/w magnetite), and the fibers were superparamagnetic at room temperature. This enabled external magnetic field control of fiber movement, rendering the material suitable for actuation applications. Notably, the fibers exhibited superior mechanical properties and actuation stresses compared to conventional fiber-based magnetic actuators. Moreover, the fibers developed herein could be used to create macroscopic systems with self-recovery shapes, underscoring their potential in soft robotics applications.

Keywords Bio-fibers · Mechanical properties · Wet-spinning · Composite · Nanomaterials · Superparamagnetism

1 Introduction

Actuators find applications in soft robotics, medical devices, and wearables. However, there is a large need for innovative, environmentally friendly materials capable of being crafted into devices with milli/micrometric dimensions [1, 2]. These materials must possess dual characteristics, inducing

Gabriele Greco and Benjamin Schmuck contributed equally to this work.

✉ Gabriele Greco
gabriele.greco@slu.se

✉ Anna Rising
anna.rising@slu.se

[1] Department of Animal Biosciences, Swedish University of Agricultural Sciences, Box 7011, 75007 Uppsala, Sweden

[2] Department of Medicine Huddinge, Karolinska Institutet, Neo, 14183 Huddinge, Sweden

[3] Department of Physics and Earth Science, University of Ferrara, Via G. Saragat 1, 44122 Ferrara, Italy

[4] Department of Industrial Engineering and INSTM Research Unit, University of Trento, via Sommarive 9, 38123 Trento, Italy

[5] Department of Civil, Environmental and Mechanical Engineering, Laboratory for Bioinspired, Bionic, Nano, Meta Materials & Mechanics, University of Trento, Via Mesiano 77, 38123 Trento, Italy

[6] School of Engineering and Materials Science, Queen Mary University of London, UK, Mile End Road, London E1 4NS, UK

[7] Instituto de Ciencia de Materiales de Madrid, ICMM/CSIC, Sor Juana Inés de la Cruz 3, 28049 Madrid, Spain

Published online: 02 October 2024

strain and exhibiting mechanical resilience while retaining strength throughout their operation [3–5]. Fibrous magnetic materials are particularly intriguing since they can generate mechanical motion without being tethered to an external power source [6–9].

Typically, synthetic polymers are used for making actuators, offering softness but often lacking high strength and Young's modulus [6, 10–12]. In this context, native silk presents a promising solution as it combines softness and desirable mechanical properties [13, 14], and indeed, native silk has shown great potential as magnetic actuator materials [15–17]. However, challenges arise from the difficulty in producing native silk materials in large quantities, attributed to the cannibalistic nature of spiders and the negative environmental impact of silkworm cultivation [18, 19]. Despite these challenges, native silk–nanomaterial composites have been designed but the need for post-spinning treatment resulted in several setbacks, e.g., excessive fiber plasticization caused by the solvent in which the nanomaterials are dispersed [14, 16, 20, 21].

An alternative to the use of native silk would be to turn to recombinant production methods to produce the silk proteins and artificially spin the silk fibers. This alternative comes with concerns related to production levels and costs [22], but recent technological advancements have showcased the scalability of producing a small genetically engineered spider silk protein (NT2RepCT) [23], so-called minispidroin, in bioreactor cultivations [24]. This minispidroin can also be purified and spun into artificial silk fibers using an eco-friendly protocol [24]. Continuous fibers made from this minispidroin have micrometric diameters, are cytocompatible [25], and they possess good mechanical properties that can be tuned by altering the spinning conditions [26, 27]. However, they lack magnetic properties, posing a challenge for actuator applications.

An interesting way forward would be to design a composite made from recombinant minispidroins and magnetic nanomaterials [28]. Preferably, the nanomaterials would be mixed with the spinning dope (soluble minispidroins) before spinning to enable the generation of composite fibers with homogeneously distributed nanomaterials, which is necessary to avoid reducing fiber's mechanical properties [29, 30]. Early attempts to spin artificial silk fibers containing nanomaterials have only resulted in fibers with compromised mechanical properties, possibly due to that the methods employed rely on harsh solvents that are incompatible with natively folded proteins [31–35]. The use of water as the sole solvent to make protein-nanomaterial composites is challenging because the nanomaterials are not easily dispersed in a range of pH 6–8. However, magnetite nanoparticles coated with meso-2,3-dimercaptosuccinic acid (DMSA) are dispersed well in aqueous solutions, also at physiologically relevant pHs [36].

Herein, we pioneer the design and manufacturing of magnetic artificial spider silk fibers using only water-based solutions. The composite fibers were easily spun at a scale of hundreds of meters and maintained their mechanical properties even at high magnetite concentrations (up to 20% w/w). Notably, they offer tunable magnetic functionality and exhibit the highest actuation stress among described magnetic fiber actuators. Their versatility extends to forming self-supporting macro devices, enhancing their potential applications.

2 Results and discussion

To achieve a uniform dispersion of nanomaterials in the protein spinning dope, we used magnetite nanoparticles that were coated with meso-2,3-dimercaptosuccinic acid (DMSA), which makes the surface negatively charged and hydrophilic [36]. The nanoparticles had a mean diameter of ~ 18 nm (Fig. S1, Table S1) and could successfully be dispersed in aqueous solutions. Composite artificial spider silk fibers were produced using the recombinant spider silk protein NT2RepCT [23], which can be produced in scalable bioreactor cultivations at significant yields (~ 15 g of pure protein per liter of microbial cell culture) and spun into artificial silk fibers with an eco-friendly protocol using water as the sole solvent [24]. Composite spinning dopes containing 0.2–20% w/w magnetite were extruded with a syringe pump via a pulled glass capillary into a bath containing an acetate buffer at pH 5 (Fig. 1a). The spinning of the protein-nanoparticle solution was continuous, which made it possible to produce hundreds of meters of fibers and collect them into bundles. Notably, the spinning process remained effective even at a magnetite concentration of 20% w/w (Fig. 1b, Supplementary video 1). This is impressive considering that previously reported manufacturing methods have resulted in silk composites with less than 2% w/w nanoparticles (Table S2). High concentrations of nanoparticles in fibrous composites can also be achieved through electrospinning [37–40]. However, these methods typically use organic solvents, such as chloroform, which further underscores the quality of our approach.

The presence of nanoparticles did not affect the overall morphology of the fibers (Fig. 2a and Fig. S2), which displayed an average diameter between 8 and 15 µm. High magnification and resolution SEM images indicated that the magnetite nanoparticles were homogeneously dispersed in the fibers (Fig. 2b and Fig. S3). Furthermore, results from energy-dispersive X-ray (EDX) analysis confirmed that iron was found in the protein matrix in a stoichiometric ratio compatible with the nominal values, even at the highest concentration (Fig. S4). This is noteworthy considering the natural tendency of nanoparticles to form agglomerates [41]

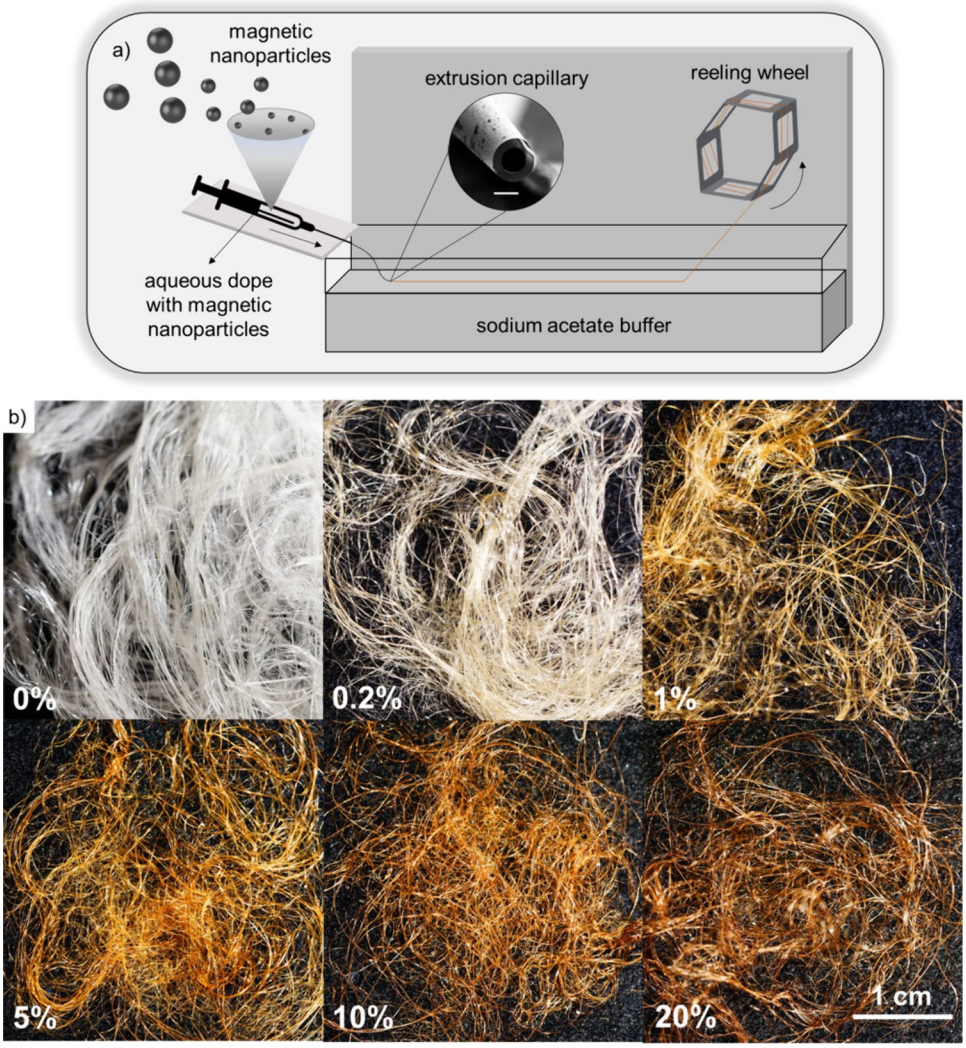

Fig. 1 Spinning of the magnetic artificial silk fibers. **a** Schematic of the spinning setup. The nanoparticles were mixed with the recombinant spider silk protein solution (300 mg/mL in Tris–HCl pH 8) to generate spinning dopes containing 0.2–20% w/w magnetite. The solutions were spun into fibers by extrusion through a glass capillary into a 0.75 M NaAc buffer at pH 5 [27]. The fibers were reeled at constant speed by a rotating wheel. The spinning was continuous and allowed the collection of bundles of magnetic silk fibers. The scale bar for the capillary in **a** is 20 µm. **b** Pictures of composite fibers containing different nominal w/w magnetite concentrations

and prompted us to obtain further evidence using magnetic measurements.

The magnetic properties of the composite fibers were studied by SQUID magnetometry methods, which also informed on inter-particle interaction effects (Figs. 3 and S5–S7, supplementary section S1). Magnetic loops were measured at different temperatures (Figs. 3a and S6), and, by comparing the value of the saturation magnetization to that of the DMSA-coated nanoparticles alone (Fig. S5), we estimated the concentration of magnetite in the fibers. These estimates were in good agreement with the nominal values for all samples (Table S3). At 300 K, no magnetic hysteresis was observed in the composite fibers, i.e., coercivity and remanent magnetization were null (Fig. 3a), in contrast to what was found at 5 K (Fig. S6). This result is compatible with a superparamagnetic behavior of the nanoparticles at room temperature. The magnetic moment of an isolated single-domain nanoparticle can undergo magnetic relaxation, possibly culminating in the superparamagnetic behavior at a critical temperature (blocking temperature) at which the thermal energy is comparable to the magnetic energy required for its reversal [42]. The onset of the superparamagnetic regime implies that the nanoparticle magnetic moment flips randomly between different spatial orientations.

Next, the magnetic relaxation of the nanoparticles in the fibers was studied through the analysis of the thermoremanent magnetization vs. temperature and corresponding temperature derivative curve [42]. The latter is a figure of the distribution of blocking temperature values for the assembly of embedded nanoparticles. In all samples, the thermoremanent magnetization went to zero with increasing temperature (Fig. 3b), confirming the progressive entrance into the superparamagnetic regime of the whole nanoparticle assembly. For magnetite concentrations up to 5% w/w, the derivative curves in Fig. 3c feature a narrow profile, and the peak temperature coincides with the blocking temperature predicted for the magnetite nanoparticles when considered individually relaxing magnetic elements (more details can be found in section S1). This indicates that the nanoparticles are homogeneously dispersed in the protein matrix and

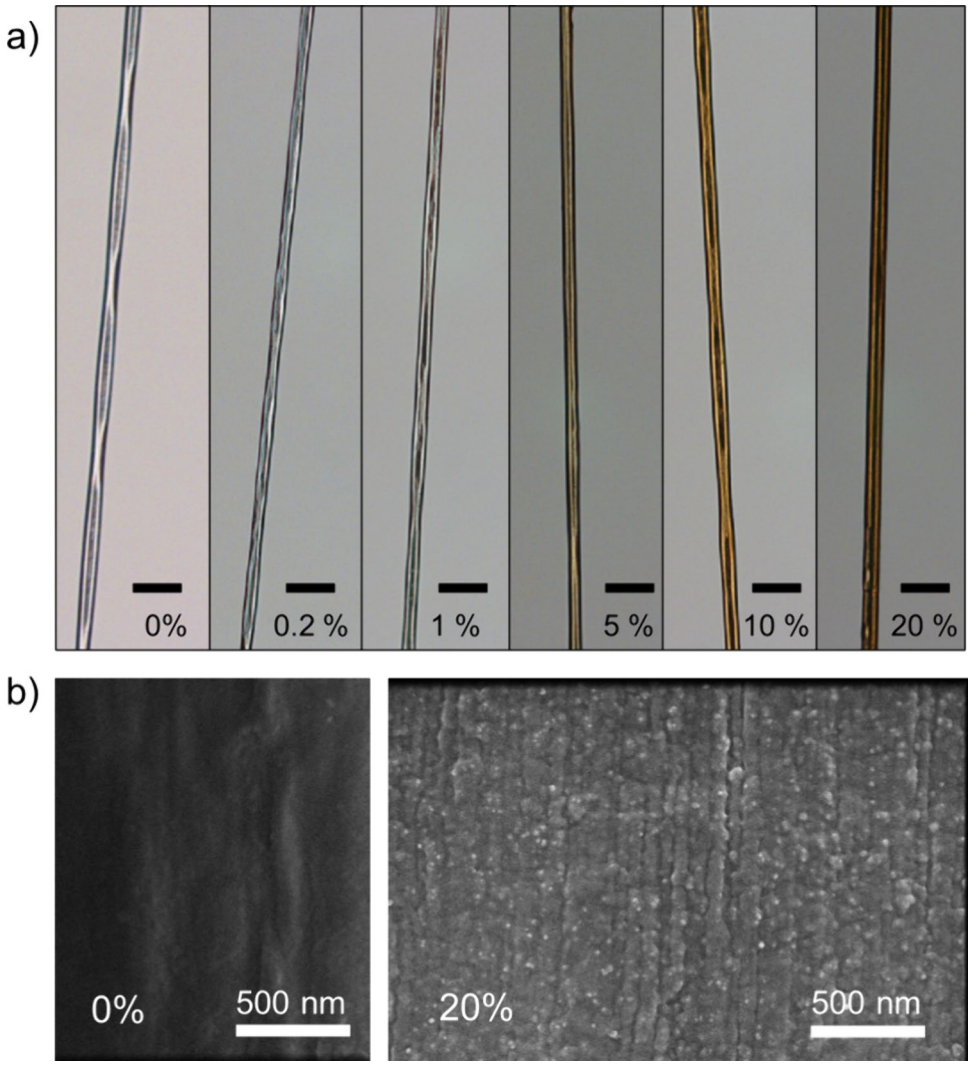

Fig. 2 **a** Representative light microscopy images of the magnetic artificial silk fibers with different nominal w/w magnetite concentrations. Scale bars are 50 µm. **b** High magnification SEM images of the NT2RepCT fibers (i.e., fibers containing no nanoparticles) and 20% w/w (nominal) of magnetite, which indicates homogeneous dispersion of the nanoparticles

sufficiently distant from each other to make dipolar interactions negligible. The derivative curves of fibers containing 10% and 20% w/w magnetite were broader and slightly shifted to higher temperatures, which is consistent with the presence of inter-particle dipolar interactions and suggests that the nanoparticles are well distributed spatially although not as homogeneously as in fibers with lower magnetite concentration [42, 43]. This was further supported by the results of the field dependence of the remanent magnetization (ΔM plots analysis at 20 K, Fig. S7). Therefore, despite inter-particle dipolar interactions, which in the samples with higher magnetite concentration slightly increase the blocking temperature, the whole nanoparticle assembly in all fibers is in the superparamagnetic regime at room temperature. This implies that the composite fibers are not permanently magnetized, but their magnetic response can be switched on and off by an external magnetic field. This could be an important property for materials intended for soft robotics applications for which the material must also have sufficient mechanical properties to withstand the stresses associated with completion of the intended task [7, 8]. For this reason, we investigated the mechanical properties of the composite fibers.

Nanomaterial composites often display reduced strength, maintained Young's modulus, and a strain at break that can be higher or lower compared to the pristine material [32, 52–59]. This is due to that the nanomaterials act as defects in the composite when there is no or poor mechanical communication between the nanomaterials and the surrounding matrix [60]. In line with this, the strength and the toughness modulus of the composite fibers were reduced compared to fibers without nanoparticles (Fig. 4a, b). Surprisingly, at magnetite concentrations higher than 0.2% w/w, no further deterioration of the strength and toughness modulus was detected (Figs. 4, S8–S9, and datasheet). The highest strain at break for all fibers investigated was obtained for fibers containing 0.2% w/w magnetite which remains to be rationalized but agrees with previous findings for silk composites (Fig. 4c, Supplementary Table S2). Young's modulus of the

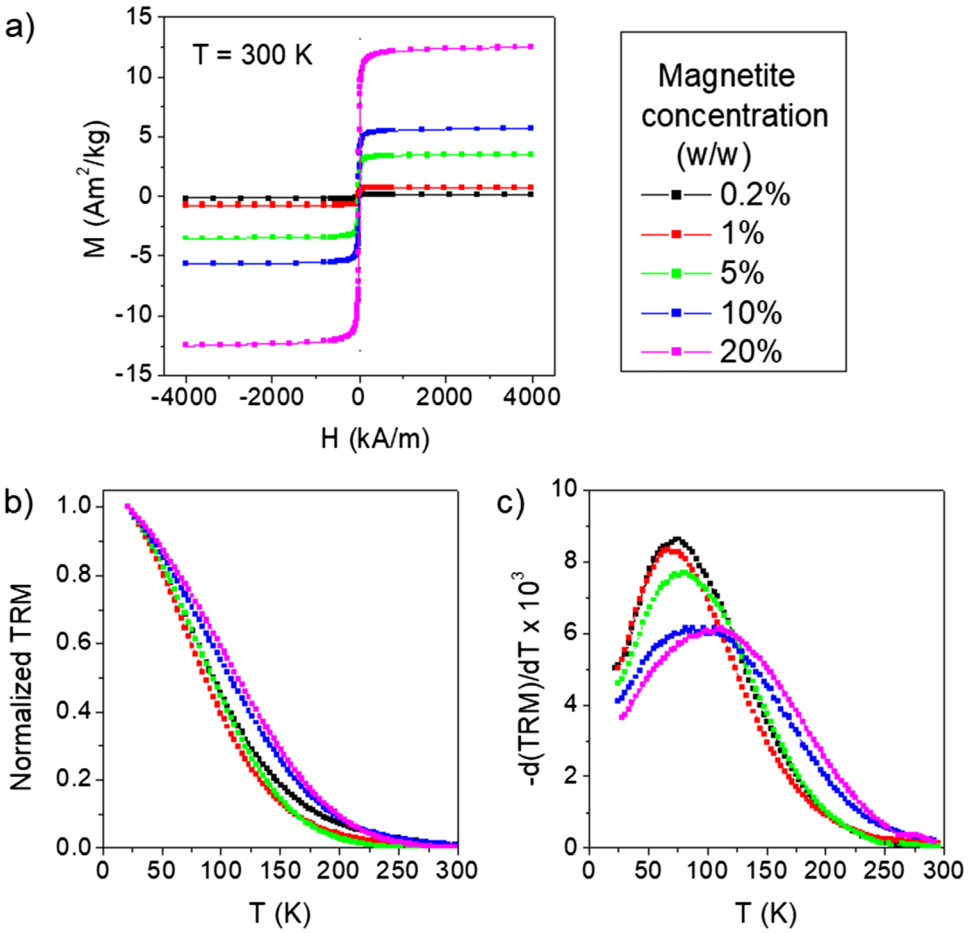

Fig. 3 Magnetic properties of the magnetic artificial silk fibers. **a** Magnetization M vs. magnetic field H measured at $T = 300$ K (curves corrected for the magnetic signal from the NT2RepCT matrix; see "Materials and methods" and Fig. S15). **b** Thermoremanent magnetization (TRM) vs. T (magnetic field previously applied to the samples $H = 4$ kA/m); the curves are normalized to their initial value at $T = 20$ K. **c** Derivatives of the curves in **b**, normalized to their area. The different colors indicate different nominal w/w magnetite concentrations

composite fibers was not significantly affected compared to that of the pristine material (Fig. 4d).

In order to better understand the effects of the nanoparticles on the mechanical properties of the composite, we analyzed our results using the model developed by Zare [29] for Young's modulus and strength of the composite fibers (see supplementary section S2, Figs. S10–S11). In this model, specific attention is devoted to the role of the interphase between the matrix (in our case NT2RepCT) and the filler (magnetite core of the nanoparticles). The interphase is in this case represented by the interface between the magnetite and the DMSA, the DMSA coating, and the interface between the DMSA and the silk proteins. According to the model, the mechanical strength and stiffness of the interphase ($\sigma_{interphase}$ and $E_{interphase}$, respectively) as well as its thickness (t, which is estimated to be less than 1 nm for our nanoparticles) influence the resulting mechanical properties of the composite material (Fig. S10a). If the strength and the stiffness of the interphase are much lower than those of the matrix, the presence of the nanoparticles (up to 20% w/w magnetite concentration) will reduce the strength of the composite while leaving Young's modulus unaffected, which agrees with the experimental data (Fig. S10b-e, see supplementary section S2 for details regarding the choice of values for $E_{interphase}$, $\sigma_{interphase}$, and t). For Young's modulus, the model shows that the values of $E_{interphase}$ must be much higher than those we used to fit the model to significantly stiffen the composite fibers with respect to the pristine material (Fig. S10b). Likewise, the concentration of magnetite has to be much higher than 20% w/w to induce a further decline of the strength of the composite fiber with respect to the pristine material, which aligns well with the experimental data (Fig. S10c–e). Thus, the experimental values we obtained for the mechanical properties of the composite fibers can be explained by the model when using low values for the interphase mechanical properties and implies that there is only a weak mechanical coupling between the nanoparticles and the surrounding protein matrix.

Another way of investigating the level of mechanical coupling between the nanoparticles and the protein matrix could be to analyze the shape of the stress-strain curves and, in particular, the presence and degree of necking. For polymeric fibers, necking is associated with the presence of defects in the material since these alter the distribution of the stress, leading to localized deformations and thus an overall reduction of the measured load [61, 62]. Indeed, the

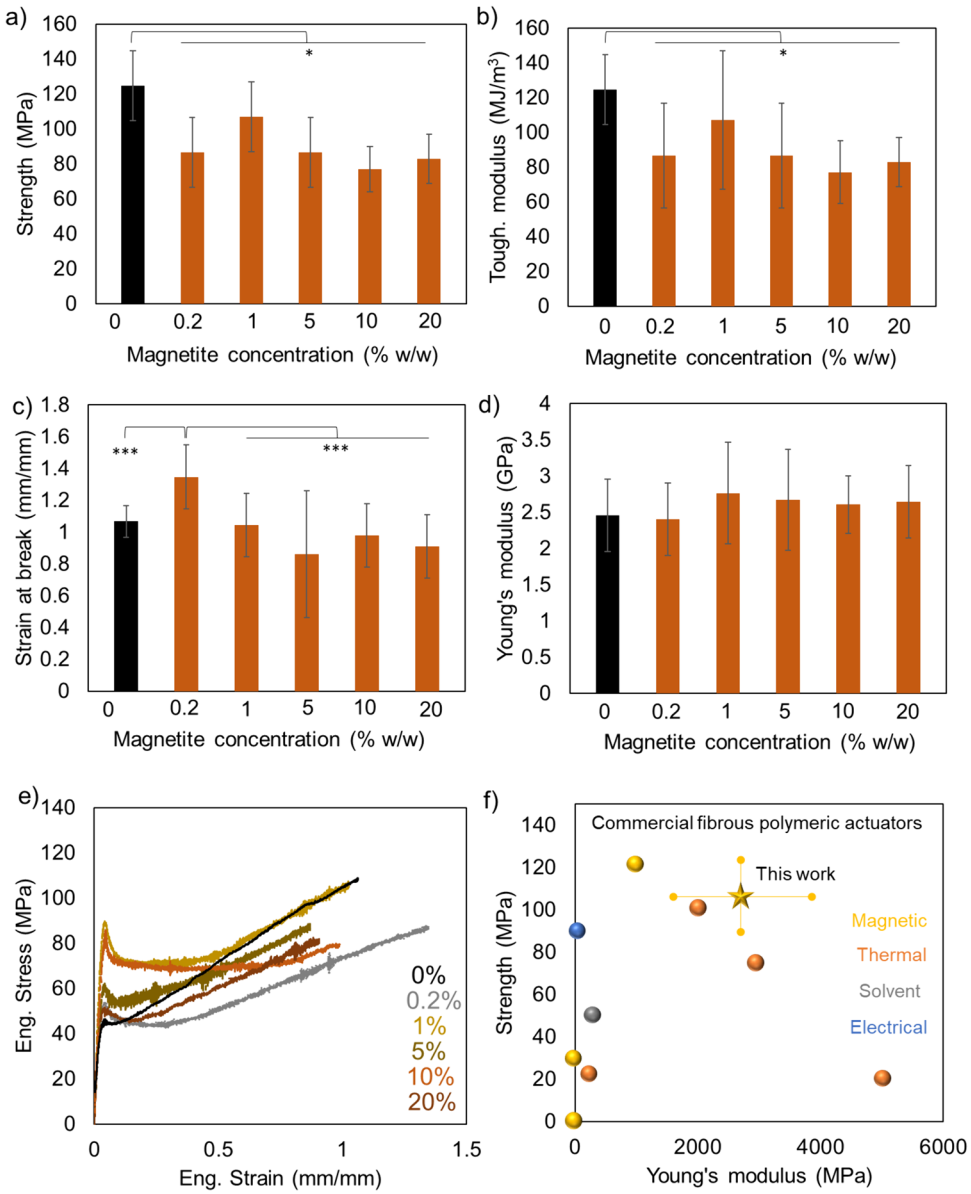

Fig. 4 Mechanical properties of the magnetic artificial silk fibers. **a** Strength, **b** toughness modulus, **c** strain at break, **d** Young's modulus. The values of the mechanical properties are here reported vs. nominal values of magnetite concentrations. Asterisk (*) indicates $p < 0.05$, $^{**}p < 0.01$, and $^{***}p < 0.001$. **e** Representative stress-strain curves of the NT2RepCT and composite fibers that were tensile tested. **f** Ashby plot of the mechanical properties of commercial polymeric fiber actuators and the mechanical properties of the actuator developed in this work. The data from the literature are from references [9, 44–51]. The actuation of the strain was induced by electrical (blue), thermal (orange), and magnetic stimuli (yellow) or when the fibers were immersed in a solvent (gray)

fibers containing the nanoparticles displayed a higher degree of necking compared to the control, supporting the idea that there is only a weak mechanical coupling between the protein matrix and the magnetite, thus reducing the strength of the composite (Fig. S12). The lack of mechanical coupling could be due to the absence of interaction between the protein matrix and the nanoparticles, which is also supported by the fact that the protein solution remained soluble after the addition of the nanoparticles. In the case of strong interactions between the two, the nanoparticles would have acted as cross-linkers, likely causing aggregation of the proteins or solidification of the spinning dope. The absence of any significant interaction between the DMSA-coated nanoparticles and the proteins was further confirmed using a surface plasmon resonance assay (see supplementary section S3 and Fig. S13). The lack of interaction also supports the notion that the nanoparticles do not alter the secondary structure of the silk in the composite fiber. For instance, a recent study on silk fibroin film mixed with iron oxide nanoparticles, using Fourier-transform infrared spectroscopy analysis, confirmed that the nanoparticles do not affect the secondary structure of the silk [63].

While the weak interactions between the nanoparticles and the protein matrix in the fibers can explain the reduced strength of the composite fibers compared to the pristine fibers, the composite fibers presented herein have outstanding mechanical properties compared to commercial fibers used for actuation in soft robotics, especially when considering magnetic actuators (Fig. 4e, f) [6–9, 44–51].

The properties of the composite fibers presented here make them interesting for applications in soft robotics. As a

proof of their usefulness, we performed magnetic actuation experiments on single fibers, using a custom-made setup presented previously [16]. From these experiments, the actuation stress generated in the composite fibers when exposed to an external magnetic field gradient was determined. In general, actuation stresses in fibers can be obtained by immersion in a solvent [15, 45, 67, 68], application of a voltage [44, 64, 65], or exposure to high temperatures [48–51, 66] or magnetic fields (Fig. 5a). When comparing the performance of our magnetic spider silk fibers to the fibrous magnetic actuators described in literature for which the actuation stress was measured, it is evident that the actuation stress mediated by our fibers is impressive (Fig. 5a) [16, 46, 47, 69]. This combined with the fibers' good mechanical properties (Fig. 4) also in relation to other materials used for actuation (Fig. 4e, f and Fig. S14) [15, 44–51, 64–69] encouraged us to build a device from a bundle of fibers and sponge cubes, which mimics a robotic finger (Fig. 5b, c). The device was self-supporting and responded to magnetic actuation (Fig. 5c and Supplementary video 2). Importantly, the induced actuation was reversible, and the system displayed a spontaneous shape recovery which is a desirable characteristic for specific actuators. This creates a solid foundation for developing future in-depth studies focused on the magnetic actuation properties of our fibers [70].

To summarize, the negative environmental impact of materials used in soft electronics and robotics has to be tackled at the design level [4, 5, 71]. In line with this, we herein present a manufacturing process of spider silk composite fibers that employ only water-based solvents and ambient temperature. The composite fibers have properties that outperform most currently used fibrous magnetic actuators and can be produced in large quantities. Given the tunable material properties, fiber dimensions, and actuation capabilities, magnetic artificial spider silk fibers should serve well for several applications in the soft robotics and related fields.

3 Concluding remarks

In this work, we develop a novel fiber—a magnetic artificial spider silk fiber—designed with a specific focus on soft robotics applications. These fibers exhibit high strength and flexibility, offering a sustainable, large-scale production process that avoids the need for harsh chemicals. Notably, their magnetic characteristics and exceptional actuating

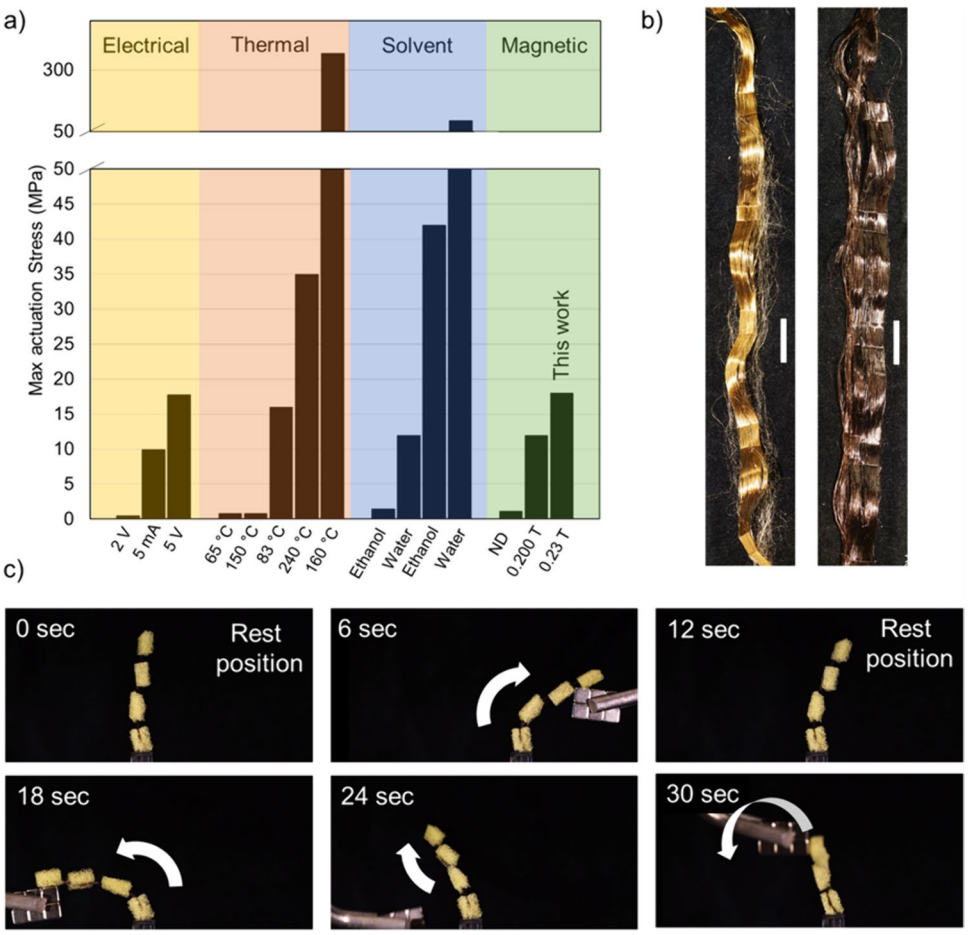

Fig. 5 Actuation properties of the magnetic artificial silk fibers. **a** Maximum actuation stresses measured for fibrous actuators induced by electrical, thermal, and magnetic stimuli or when the fibers were immersed in a solvent. ND means that the actuating magnetic field was not declared. The material presented in this work has the highest actuation stress among magnetic fibrous actuators. The data were obtained from the following references [15, 44–51, 64–68]. **b** Bundles of magnetic artificial silk fibers. Scale bars are 2 cm. **c** Proof of concept that the magnetic fibers can be used for the design of a macroscopic actuator device. In this case, a bundle of magnetic silk fibers (10% w/w magnetite concentration) was activated by a magnet which induced a finger-like motion. When the magnet was removed, the fiber bundles retained their original shape

stress levels surpass the performance of conventional fibrous magnetic actuators. Consequently, these fibers possess the essential attributes necessary for a wide range of applications, particularly in scenarios demanding untethered device operation.

4 Materials and methods

4.1 Synthesis and coating of the nanoparticles

Nanoparticles were produced and coated as described in Ovejero et al. [72] and Roca et al. [73], respectively. Briefly, magnetite nanoparticles were synthesized by thermal decomposition of $Fe(acac)_3$ in the presence of oleic acid and oleylamine as surfactants and organic solvents with different boiling points. In particular, iron(III) acetylacetonate 99% (Acros Organics, Geel, Belgium) was decomposed in benzyl ether (99%; Acros Organics, Geel, Belgium) in the presence of oleic acid (OA; 80%; GPR Rectapur®, VWR, Leicestershire) and 1,2-dodecanediol 90% (ODA; Sigma-Aldrich, San Luis, MO, USA). We used a molar ratio of 1:3:2 ($Fe(acac)_3$:OA:ODA) and a concentration of the iron precursor of 0.1 M. The solution was heated up to 200 °C for 120 min with mechanical stirring and under a nitrogen flow. Then, we heated the solution to reflux (bp 254 °C) for 30 min in an N_2 atmosphere. Once at room temperature, the solution was mixed with ethanol and centrifuged at 5650 g for 10 min. The supernatant was then discarded. Lastly, we mixed the nanoparticles with 40 mL of hexane and 0.1 mL of oleic acid and centrifuged twice at 5650 *g* for 10 min. After this, we obtained a stable hydrophobic suspension. Then, we employed a ligand exchange reaction of oleic acid for dimercaptosuccinic acid (DMSA) to make magnetite nanoparticles hydrophilic and thus dispersible in water. We first coagulated the nanoparticles from the hydrophobic suspension by adding ethanol and centrifugation at 2825 *g* for 10 min to eliminate the solution. Then, we added a solution of toluene (25 mL) and a solution of 90 mg DMSA in 5 mL of dimethyl sulfoxide (DMSO) sonicated for 5 min and mechanically stirred for 24 h. Then, we added toluene and centrifuged again, discarding the supernatant containing the oleic acid–coated particles. We then mixed and centrifuged with ethanol and acetone several times to remove the free oleic acid molecules. The nanoparticles were then dispersed in alkaline water and then dispersed at pH 7. The dispersion was then dialyzed and filtered through a 0.2 µm pore size syringe.

The magnetite nanoparticles were characterized by transmission electron microscopy (TEM, JEOL JEM 1011, Peabody, MA, USA), X-ray powder diffraction (XRD, Bruker D8 Advance, Billerica, MA, USA), thermogravimetric analysis (TG-DTA, Q600 TA Instruments, New Castle, DE 19720, USA), and photon correlation spectroscopy (PCS, Zetasizer Nano, Malvern Panalytical, Malvern, UK) (Fig. S1, Table S1).

4.2 Spinning the artificial silk (w and w/o nanoparticles)

The minispidroin NT2RepCT [23] (with 6xHis-tag) was expressed in a bioreactor in a fed-batch culture and purified in native conditions with a 20 mM Tris–HCl buffer at pH 8 and by using immobilized ion metal chromatography (IMAC) as described earlier [24]. After elution of NT2RepCT from the IMAC column with 20 mM Tris–HCl and 200 mM imidazole, NT2RepCT was dialyzed against 20 mM Tris–HCl (pH 8). To prepare the spinning dope, NT2RepCT was concentrated to ~ 300 mg/mL (which represents an optimum in order to maximize the mechanical properties of the fiber [27]) with an Amicon Ultra-15 centrifugal filter unit (Merck-Millipore, Darmstadt, Germany) at 4000 × g and 4 °C using an ultracel-10 membrane (10 kDa cutoff). After recovering the spinning dope from the centrifugal filter unit and transferring 500 µL to a new filter unit, DMSA-coated magnetite nanoparticles in an H_2O suspension (12–50 mg/mL Fe_3O_4) were added. The NT2RepCT and magnetite blend were re-concentrated to a final volume of 500 µL, corresponding to the original volume of the spinning dope before adding the magnetite suspension to the centrifugal filter unit. Although it was difficult to judge due to the very viscous consistency and blackness of the spinning dope, independent of the nanoparticle concentration, no agglomerates were observed with the naked eye. Thus, the dope was prepared in a way to expect a final protein concentration of 300 mg/mL in the spinning dope, while expecting a magnetite (Fe_3O_4) concentration in the dry fiber of 0.2%, 1%, 5%, 10%, or 20% w/w. Then, the final dope was transferred into a 1-mL syringe with a Luer lock tip (BD, Franklin Lakes, NJ, USA). To make fibers, a recently developed optimized spinning protocol was used [27]. The syringe with the spinning dope was mounted in a neMESYS low-pressure (290 N) syringe pump (CETONI, Korbußen, Germany) where it was connected to a pulled glass capillary via polyethylene tubing. The glass capillary had a tapered tip with an orifice diameter of 50 ± 10 µm and was used to extrude the NT2RepCT/magnetite blend into a spinning bath containing 4 L 0.75 M acetate (Na) at pH 5. As soon as the spinning dope entered the spinning bath, it solidified, and a fiber was formed. The fibers were continuously collected at the end of the 0.8 m long bath with a rotating wheel at 0.58 m/s.

4.3 SEM and EDX

A Zeiss SUPRA 40 field emission scanning electron microscope was used to investigate the morphology of the fibers with the secondary electron detectors. The samples were coated with an alloy Pt:Pd (80:20) utilizing a Quora Q150 and mounted on a standard Zeiss stab. Further, SEM and EDX characterization was performed with a FEI VERIOS 460 and an EDAX Octane Plus.

4.4 Magnetic measurement

The magnetic study was carried out using a Quantum Design MPMS-XL superconducting quantum interference device (SQUID) magnetometer, which can measure the magnetic moment of a sample as a function of magnetic field (maximum applied field $H = 4 \times 10^3$ kA/m) and temperature T (5–300 K range). To calculate the magnetization M (magnetic moment/sample mass), the mass of the sample was measured with a precision of 10^{-8} kg. The fibers loaded with DMSA-coated nanoparticles were measured by taking a certain amount of material and manually forming a small bundle, which was inserted directly into the sample holder for SQUID supplied by Quantum Design. NT2RepCt fibers without magnetic nanoparticles were also analyzed as reference material; DMSA-coated nanoparticles alone were measured in powder form.

The spidroin matrix exhibited a paramagnetic behavior at very low temperatures, while at $T = 300$ K a diamagnetic signal predominated (Fig. S15). Therefore, to estimate the weight fractions of magnetite in the fibers, first, the hysteresis loops of the samples—particularly those with low magnetic load, i.e. 0.2% and 1% w/w—were corrected for the magnetic signal of the spidroin matrix; then, the M_S values at $T = 300$ K were compared to that obtained for the magnetite phase in the nanoparticles alone at the same temperature (M_S at $T = 300$ K was considered to minimize the influence of the low-temperature paramagnetic signal from the spidroin matrix, which, being temperature dependent, was rather difficult to reliably remove from the measured loops).

The thermoremanent magnetization (TRM) was measured following this procedure: the sample was cooled from $T = 300$ K down to $T = 20$ K in an applied magnetic field $H = 4$ kA/m. At $T = 20$ K, the field was removed, and the remanent magnetization was measured as a function of the increasing temperature up to 300 K (heating rate = 3 K/min). The recorded TRM curve was normalized to its initial value.

The ΔM plots were built starting from the curves of isothermal remanent magnetization (IRM) and dc demagnetization remanence (DCD), measured at $T = 20$ K using a standard procedure [43]. In particular, in the IRM measurement procedure, an initially demagnetized sample is progressively magnetized by a positive magnetic field increasing from 0 kA/m up to 1.6×10^3 kA/m. The recorded remanence values are plotted as a function of the previously applied magnetic field, and the obtained curve is normalized to its final value. The DCD measurement is similar except that initially the sample is negatively saturated and the curve of remanence vs. H is normalized to its initial value (Fig. S16). The ΔM plot is obtained by plotting the parameter $\Delta M(H) = DCD(H) - [1 - 2\ IRM(H)]$ as a function of H (see supplementary section S1).

4.5 Mechanical measurement

All the fibers were tested at room temperature and 25–30% relative humidity (RH) 2 weeks after they were spun. During this period, they were stored in a dry cabinet (Dry Keeper SUNPLATEC) below 20% RH. Single fibers were mounted on paper frames (1 × 1 cm open square window) providing a ~ 1 cm gauge length. The fiber diameter was measured in five randomly picked spots by means of light microscopy and then averaged as previously described. An Instron Single Column 5943 was used to tensile test the artificial silk fibers, with a strain rate of 6 mm/min. The engineering stress was calculated assuming a circular cross-sectional area. From the engineering stress and strain curves, Young's modulus was obtained from linear regression in the initial elastic part of the curve (by 2% of strain); the strength was obtained as the stress at fracture and the toughness modulus as the area under the curve. The tested fibers were obtained from at least 3–5 different spinning occasions, from which we tested at least 10 fibers. Thus, the mechanical properties reported in this study represent an average of 30–50 fibers. Single one-tail pairwise ANOVA was run with Excel®.

4.6 Light microscopy

Light microscopy inspection was performed using a Nikon Eclipse Ts2R-FL microscope equipped with a DFKN-ME33UX264 5 MP camera and a CFI Plan Fluor DL-10X objective. The captured images and the diameters were measured with Nikon NIS-Elements BR software.

4.7 Measurement of the density of the fibers

Density measurements of about 35 mg of NT2RepCT fibers were carried out in a Micromeritics® AccuPyc 1330 helium pycnometer (Norcross USA), at 23.0 °C, performing at least 99 measurements.

4.8 Surface plasmon resonance (SPR) assay

To study if there is an interaction between the DMSA-coated nanoparticles and NT2RepCT, we set up an SPR assay using a Biacore 8 K + (Cytiva) and with a Ni^{2+}-charged

carboxymethylated dextran pre-immobilized with nitrilotriacetic acid (NTA) Sensor S type chip (Cytiva). The instrument was controlled, and the assay was designed with the Biacore 8 K control software version 3.0.12.15655. The immobilization of NT2RepCT on the NTA-coated gold surface was achieved with the 6xHis-tag. We have not chosen covalent coupling methods usually employed to immobilize the ligand in SPR assays due to the pH sensitivity of NT2RepCT.

The temperature of the system was 25 °C throughout the entire experiment. To immobilize, 0.5 M $NiCl_2$ (NTA Reagent Kit, Cytiva) was injected with a contact time of 60 s at a flow rate of 10 µL/min, after which the surface was washed with a running buffer containing 3 mM EDTA. Thirty-five micromolar NT2RepCT dimer was captured with a contact time of 300 s also at a flow rate of 10 µL/min. A maximal immobilization level of 8000 RU when the running buffer was HSB-N (Cytiva) or 3000 RU with 20 mM Tris-HCl buffer (pH 8) was reached. On the reference surface, no nickel was injected to not capture the ligand and detect unspecific binding of ligand and analyte.

Analyte solution with a magnetite concentration of 4.5 µg/mL, 0.45 µg/mL, and 0.045 µg/mL was injected over the surface with a contact time of 120 s and a dissociation time of 600 s at 30 µL/min. Regeneration of the chip surface was achieved with 350 mM EDTA (NTA Reagent Kit, Cytiva), using a contact time of 60 s and a flow rate of 30 µL/min.

4.9 Magnetic actuation measurements

The magnetic actuation measurements were done with the same custom-made setup reported by Spizzo et al. [16]. Briefly, the fibers were kept in tension (0.5% strain level) with the support of Agilent Technologies T150 UTM. A commercial set of cubic nickel-plated N42 NdFeB magnets was used to create a non-uniform magnetic field to apply a drag force to the fiber. The intensity of the magnetic field was measured using a FW-Bell 9500 Gaussmeter using a 1-axis Hall probe (the maximum magnetic induction field achieved was $B = 0.23$ T). During the approaching of the magnet, the load on the fiber was recorded with the Agilent technologies T150 UTM. The load recorded was converted in engineering stress assuming the cross-section circular. Every measurement was repeated five times per fiber.

Supplementary information The online version contains supplementary material available at https://doi.org/10.1007/s42114-024-00962-y.

Acknowledgements N.M.P., L.F., and G.G. thank Professor Antonella Motta for the help with the scanning electron microscopy facility. We also want to thank the Testa Center in Uppsala for providing access to the Biacore 8 K + and Ewa Pol from Cytiva for advice on setting up the SPR assay. Finally, authors acknowledge the Scanning Electron Microscopy Service at the Instituto de Micro y Nanotecnología (IMN-CSIC) for FESEM and the Ministerio de Ciencia e Innovación of Spain for PID2020-113480RB-I00 grant.

Author contribution G.G., N.M.P., and A.R. conceived the idea and supervised the project. B.S. produced the protein, prepared the spinning dope, performed spinning, and conducted the SPR assay. M.P.M. and S.V-V. prepared and structurally characterized the magnetic nanoparticles and performed SEM and EDX. L.D.B. and F.S. conducted the magnetic study. G.G. and B.S. conducted tensile testing. G.G. obtained light microscopy and SEM images of the morphology, curated the analytical model, and performed the actuation experiments. L.F. performed the density experiments. All authors contributed to the analysis and discussion of the data. G.G., B.S., L.D.B., F.S., and A.R. wrote the first draft of the manuscript, and all authors contributed to the editing process. All authors have approved the final version of the manuscript.

Funding Open access funding provided by Swedish University of Agricultural Sciences. This work was supported by the European Research Council (ERC) under the European Union's Horizon 2020 research and innovation program (grant agreement No 815357), the Center for Innovative Medicine (CIMED) at Karolinska Institutet and Stockholm City Council, and the Swedish Research Council (2019–01257) to A.R. N.M.P. is supported by the European Commission under the FET Proactive ("Boheme") Grant No. 863179. G.G. was supported by Wenner-Gren Stiftelse (UPD2021-0047) and by the project "EPASS" under the HORIZON TMA MSCA Postdoctoral Fellowships—European Fellowships (project number 101103616). The research work of L.D.B. and F.S. was supported by the University of Ferrara under projects 2022-FIRD and 2023-FIRD.

Data availability All the data necessary to understand the content of this work are reported in the main manuscript, the supplementary material, and additional datasheet files.

Declarations

Competing interests The authors declare no competing interests.

References

1. Sitti M (2018) Miniature soft robots - road to the clinic. Nat Rev Mater 3:74–75. https://doi.org/10.1038/s41578-018-0001-3
2. Gates BD (2009) Flexible electronics. Science 323:1566–1567. https://doi.org/10.1126/science.1171230
3. Yang GZ, Fischer P, Nelson B (2017) New materials for next-generation robots. Sci Robot 2:1–3. https://doi.org/10.1126/scirobotics.aap9294
4. McCulloch I, Chabinyc M, Brabec C, Nielsen CB, Watkins SE (2023) Sustainability considerations for organic electronic

products. Nat Mater 22:1304–1310. https://doi.org/10.1038/s41563-023-01579-0
5. (2023) Electronics can be more sustainable. Nat Mater 22:1273. https://doi.org/10.1038/s41563-023-01731-w
6. Rich SI, Wood RJ, Majidi C (2018) Untethered soft robotics. Nat Electron 1:102–112. https://doi.org/10.1038/s41928-018-0024-1
7. Kim Y, Zhao X (2022) Magnetic soft materials and robots. Chem Rev 122:5317–5364. https://doi.org/10.1021/acs.chemrev.1c00481
8. Xiong J, Chen J, Lee PS (2020) Functional fibers and fabrics for soft robotics, wearables, and human–robot interface. Adv Mater 33:1–43. https://doi.org/10.1002/adma.202002640
9. Lee Y, Koehler F, Dillon T, Loke G, Kim Y, Marion J, Antonini M-J, Garwood IC, Sahasrabudhe A, Nagao K, Zhao X, Fink Y, Roche ET, Anikeeva P (2023) Magnetically actuated fiber-based soft robots. Adv Mater 35. https://doi.org/10.1002/adma.202301916
10. Kim SY, Baines R, Booth J, Vasios N, Bertoldi K, Kramer-Bottiglio R (2019) Reconfigurable soft body trajectories using unidirectionally stretchable composite laminae. Nat Commun 10:1–8. https://doi.org/10.1038/s41467-019-11294-7
11. Zhang Y, Wang Q, Yi S, Lin Z, Wang C, Chen Z, Jiang L (2021) 4D printing of magnetoactive soft materials for on-demand magnetic actuation transformation. ACS Appl Mater Interfaces 13:4174–4184. https://doi.org/10.1021/acsami.0c19280
12. Wang Z, Wu Y, Wu D, Sun D, Lin L (2022) Soft magnetic composites for highly deformable actuators by four-dimensional electrohydrodynamic printing. Compos Part B Eng 231:109596. https://doi.org/10.1016/j.compositesb.2021.109596
13. Omenetto FG, Kaplan DL (2010) New opportunities for an ancient material. Science 329:528–531. https://doi.org/10.1126/science.1188936
14. Wang Y, Guo J, Zhou L, Ye C, Omenetto FG, Kaplan DL, Ling S (2018) Design, fabrication, and function of silk-based nanomaterials. Adv Funct Mater 28:1–24. https://doi.org/10.1002/adfm.201805305
15. Jia T, Wang Y, Dou Y, Li Y, de Andrade MJ, Wang R, Fang S, Li J, Yu Z, Qiao R, Liu Z, Cheng Y, Su Y, Minary-Jolandan M, Baughman RH, Qian D, Liu Z (2019) Moisture sensitive smart yarns and textiles from self-balanced silk fiber muscles.pdf. Adv Funct Mater 29. https://doi.org/10.1002/adfm.201808241
16. Spizzo F, Greco G, Del Bianco L, Coïsson M, Pugno NM (2022) Magnetostrictive and electroconductive stress-sensitive functional spider silk. Adv Funct Mater 1–14. https://doi.org/10.1002/adfm.202207382
17. Reizabal A, Costa CM, Pereira N, Pérez-Álvarez L, Vilas-Vilela JL, Lanceros-Méndez S (2020) Silk fibroin based magnetic nanocomposites for actuator applications. Adv Eng Mater 22. https://doi.org/10.1002/adem.202000111
18. Astudillo MF, Thalwitz G, Vollrath F (2014) Life cycle assessment of Indian silk. J Clean Prod 81:158–167. https://doi.org/10.1016/j.jclepro.2014.06.007
19. Basu A (2015) Advances in silk science and technology. The Textile Institute, Boston
20. Steven E, Saleh WR, Lebedev V, Acquah SFA, Laukhin V, Alamo RG, Brooks JS (2013) Carbon nanotubes on a spider silk scaffold. Nat Commun 4:1–8. https://doi.org/10.1038/ncomms3435
21. Mayes EL, Vollrath F, Mann S (1998) Fabrication of magnetic spider silk and other silk-fiber composites using inorganic nanoparticles. Adv Mater 10:801–805. https://doi.org/10.1002/(SICI)1521-4095(199807)10:10%3c801::AID-ADMA801%3e3.0.CO;2-I
22. Edlund AM, Jones J, Lewis R, Quinn JC (2018) Economic feasibility and environmental impact of synthetic spider silk production from Escherichia coli. New Biotechnol 42:12–18. https://doi.org/10.1016/j.nbt.2017.12.006
23. Andersson M, Jia Q, Abella A, Lee XY, Landreh M, Purhonen P, Hebert H, Tenje M, Robinson CV, Meng Q, Plaza GR, Johansson J, Rising A (2017) Biomimetic spinning of artificial spider silk from a chimeric minispidroin. Nat Chem Biol 13:262–264. https://doi.org/10.1038/nchembio.2269
24. Schmuck B, Greco G, Barth A, Pugno NM, Johansson J, Rising A (2021) High-yield production of a super-soluble miniature spidroin for biomimetic high-performance materials. Mater Today 1–8. https://doi.org/10.1016/j.mattod.2021.07.020
25. Hansson ML, Chatterjee U, Francis J, Arndt T, Broman C, Johansson J, Sköld MK, Rising A (2021) Artificial spider silk supports and guides neurite extension in vitro. FASEB J 35:1–14. https://doi.org/10.1096/fj.202100916R
26. Greco G, Francis J, Arndt T, Schmuck B, Bäcklund FG, Barth A, Johansson J, Pugno NM, Rising A (2020) Properties of biomimetic artificial spider silk fibers tuned by PostSpin bath incubation. Molecules 25(14):3248. https://doi.org/10.3390/molecules25143248
27. Schmuck B, Greco G, Bäcklund FG, Pugno NM, Johansson J, Rising A (2022) Impact of physio-chemical spinning conditions on the mechanical properties of biomimetic spider silk fibers. Commun Mater. https://doi.org/10.1038/s43246-022-00307-6
28. Schmuck B, Greco G, Pessatti TB, Sonavane S, Langwallner V, Arndt T, Rising A (2023) Strategies for making high-performance artificial spider silk fibers. Adv Funct Mater. https://doi.org/10.1002/adfm.202305040
29. Zare Y (2016) The roles of nanoparticles accumulation and interphase properties in properties of polymer particulate nanocomposites by a multi-step methodology. Compos Part A Appl Sci Manuf 91:127–132. https://doi.org/10.1016/j.compositesa.2016.10.003
30. Mikhalchan A, Vilatela JJ (2019) A perspective on high-performance CNT fi bres for structural composites. Carbon N Y 150:191–215. https://doi.org/10.1016/j.carbon.2019.04.113
31. Pan L, Wang F, Cheng Y, Leow WR, Zhang YW, Wang M, Cai P, Ji B, Li D, Chen X (2020) A supertough electro-tendon based on spider silk composites. Nat Commun 11:1–9. https://doi.org/10.1038/s41467-020-14988-5
32. Fang G, Zheng Z, Yao J, Chen M, Tang Y, Zhong J, Qi Z, Li Z, Shao Z, Chen X (2015) Tough protein-carbon nanotube hybrid fibers comparable to natural spider silks. J Mater Chem B 3:3940–3947. https://doi.org/10.1039/c5tb00448a
33. Zhang M, Wang C, Wang Q, Jian M, Zhang Y (2016) Sheath-core graphite/silk fiber made by dry-meyer-rod-coating for wearable strain sensors. ACS Appl Mater Interfaces 8:20894–20899. https://doi.org/10.1021/acsami.6b06984
34. Hu X, Li J, Bai Y (2017) Fabrication of high strength graphene/regenerated silk fibroin composite fibers by wet spinning. Mater Lett 194:224–226. https://doi.org/10.1016/j.matlet.2017.02.057
35. Cheng J, Hu C, Gan C, Xia X, Qian Z (2022) Functionalization and reinforcement of recombinant spider dragline silk fibers by confined nanoparticle formation. ACS Biomater Sci Eng. https://doi.org/10.1021/acsbiomaterials.2c00209
36. Salas G, Casado C, Teran FJ, Miranda R, Serna CJ, Morales MP (2012) Controlled synthesis of uniform magnetite nanocrystals with high-quality properties for biomedical applications. J Mater Chem 22:21065–21075. https://doi.org/10.1039/c2jm34402e
37. Miyauchi M, Simmons TJ, Miao J, Gagner JE, Shriver ZH, Aich U, Dordick JS, Linhardt RJ (2011) Electrospun polyvinylpyrrolidone fibers with high concentrations of ferromagnetic and superparamagnetic nanoparticles. ACS Appl Mater Interfaces 3:1958–1964. https://doi.org/10.1021/am200187x
38. Roskov KE, Atkinson JE, Bronstein LM, Spontak RJ (2012) Magnetic field-induced alignment of nanoparticles in electrospun microfibers. RSC Adv 2:4603–4607. https://doi.org/10.1039/c2ra20489d

39. Brito-Pereira R, Correia DM, Ribeiro C, Francesko A, Etxebarria I, Pérez-Álvarez L, Vilas JL, Martins P, Lanceros-Mendez S (2018) Silk fibroin-magnetic hybrid composite electrospun fibers for tissue engineering applications. Compos Part B Eng 141:70–75. https://doi.org/10.1016/j.compositesb.2017.12.046
40 Strassburg S, Mayer K, Scheibel T (2021) Functionalization of biopolymer fibers with magnetic nanoparticles. In: Odenbach S (ed) Magnetic hybrid-materials: multi-scale modelling, synthesis, and applications. De Gruyter, Berlin/Boston, pp 167–193. https://doi.org/10.1515/9783110569636-007
41. Al-Hamadani YAJ, Chu KH, Son A, Heo J, Her N, Jang M, Park CM, Yoon Y (2015) Stabilization and dispersion of carbon nanomaterials in aqueous solutions: a review. Sep Purif Technol 156:861–874. https://doi.org/10.1016/j.seppur.2015.11.002
42 Dormann JL, Fiorani D, Tronc E (2007) Magnetic relaxation in fine-particle systems. In: Prigogine I, Rice SA (eds) Advances in chemical physics, vol XCVIII. Wiley, New York, pp 283–494. https://doi.org/10.1002/9780470141571.ch4
43. Del Bianco L, Spizzo F, Barucca G, Ruggiero MR, GeninattiC-rich S, Forzan M, Sieni E, Sgarbossa P (2019) Mechanism of magnetic heating in Mn-doped magnetite nanoparticles and the role of intertwined structural and magnetic properties. Nanoscale 11:10896–10910. https://doi.org/10.1039/c9nr03131f
44. Lee JA, Kim YT, Spinks GM, Suh D, Lepró X, Lima MD, Baughman RH, Kim SJ (2014) All-solid-state carbon nanotube torsional and tensile artificial muscles. Nano Lett 14:2664–2669. https://doi.org/10.1021/nl500526r
45. Wang W, Xiang C, Liu Q, Li M, Zhong W, Yan K, Wang D (2018) Natural alginate fiber-based actuator driven by water or moisture for energy harvesting and smart controller applications. J Mater Chem A 6:22599–22608. https://doi.org/10.1039/c8ta08064j
46. Lee DW, Kim SH, Kozlov ME, Lepró X, Baughman RH, Kim SJ (2018) Magnetic torsional actuation of carbon nanotube yarn artificial muscle. RSC Adv 8:17421–17425. https://doi.org/10.1039/c8ra01040d
47. Kim Y, Yuk H, Zhao R, Chester SA, Zhao X (2018) Printing ferromagnetic domains for untethered fast-transforming soft materials. Nature 558:274–291. https://doi.org/10.1038/s41586-018-0185-0
48. Ionov L, Stoychev G, Jehnichen D, Sommer JU (2017) Reversibly actuating solid janus polymeric fibers. ACS Appl Mater Interfaces 9:4873–4881. https://doi.org/10.1021/acsami.6b13084
49. Haines CS, Lima MD, Li N, Spinks GM, Foroughi J, Madden JDW, Kim SH, Fang S, De Andrade MJ, Göktepe F, Göktepe Ö, Mirvakili SM, Naficy S, Lepró X, Oh J, Kozlov ME, Kim SJ, Xu X, Swedlove BJ, Wallace GG, Baughman RH (2014) Artificial muscles from fishing line and sewing thread. Science 343:868–872. https://doi.org/10.1126/science.1246906
50. Lima MD, Li N, De Andrade MJ, Fang S, Oh J, Spinks GM, Kozlov ME, Haines CS, Suh D, Foroughi J, Kim SJ, Chen Y, Ware T, Shin MK, Machado LD, Fonseca AF, Madden JDW, Voit WE, Galvão DS, Baughman RH (2012) Electrically, chemically, and photonically powered torsional and tensile actuation of hybrid carbon nanotube yarn muscles. Science 338:928–932. https://doi.org/10.1126/science.1226762
51. Saed MO, Ambulo CP, Kim H, De R, Raval V, Searles K, Siddiqui DA, Cue JMO, Stefan MC, Shankar MR, Ware TH (2019) Molecularly-engineered 4D-printed liquid crystal elastomer actuators.pdf. Adv Funct Mater 29. https://doi.org/10.1002/adfm.201806412
52. Xu H, Yi W, Li D, Zhang P (2019) Obtaining high mechanical performance silk fibers by feeding purified carbon nanotube / lignosulfonate composite to silkworms †. RSC Adv 9:3558–3569. https://doi.org/10.1039/c8ra09934k
53. He W, Qian D, Wang Y, Zhang G, Cheng Y, Hu X, Wen K, Wang M, Liu Z, Zhou X, Zhu M (2022) Protein-like nanogel for spinning hierarchically structured artificial spider silk. Adv Mater. https://doi.org/10.1002/adma.202201843
54. Zhu H, Sun Y, Yi T, Wang S, Mi J, Meng Q (2020) Tough synthetic spider-silk fibers obtained by titanium dioxide incorporation and formaldehyde cross-linking in a simple wet-spinning process. Biochimie 175:77–84. https://doi.org/10.1016/j.biochi.2020.05.003
55. Yao J, Chen S, Chen Y, Wang B, Pei Q, Wang H (2017) Macrofibers with high mechanical performance based on aligned bacterial cellulose nanofibers. ACS Appl Mater Interfaces 9:20330–20339. https://doi.org/10.1021/acsami.6b14650
56. Lu L, Fan S, Niu Q, Peng Q, Geng L, Yang G, Shao H, Hsiao BS, Zhang Y (2019) Strong silk fibers containing cellulose nanofibers generated by a bioinspired microfluidic chip. ACS Sustain Chem Eng 7:14765–14774. https://doi.org/10.1021/acssuschemeng.9b02713
57. Ayutsede J, Gandhi M, Sukigara S, Ye H, Hsu C, Gogotsi Y, Ko F (2006) Carbon nanotube reinforced Bombyx mori silk nanofibers by the electrospinning process. Biomacromolecules 7:208–214. https://doi.org/10.1021/bm0505888
58. Pan H, Zhang Y, Hang Y, Shao H, Hu X, Xu Y, Feng C (2012) Significantly reinforced composite fibers electrospun from silk fibroin/carbon nanotube aqueous solutions. Biomacromolecules. https://doi.org/10.1021/bm300877d
59. Zhang C, Zhang Y, Shao H, Hu X (2016) Hybrid silk fibers dry-spun from regenerated silk fibroin/graphene oxide aqueous solutions. ACS Appl Mater Interfaces 8:3349–3358. https://doi.org/10.1021/acsami.5b11245
60. Goutianos S, Peijs T (2021) On the low reinforcing efficiency of carbon nanotubes in high-performance polymer fibres. Nanocomposites 7:53–69. https://doi.org/10.1080/20550324.2021.1917815
61. Séguéla R (2007) On the natural draw ratio of semi-crystalline polymers: review of the mechanical, physical and molecular aspects. Macromol Mater Eng 292:235–244. https://doi.org/10.1002/mame.200600389
62. Greco G, Schmuck B, Jalali SK, Pugno NM, Rising A (2023) Influence of experimental methods on the mechanical properties of silk fibers: a systematic literature review and future road map. Biophys Rev 4. https://doi.org/10.1063/5.0155552
63. Del Bianco L, Spizzo F, Yang Y, Greco G, Gatto ML, Barucca G, Pugno M, Motta A (2022) Silk fibroin films with embedded magnetic nanoparticles: evaluation of the magneto-mechanical stimulation effect on osteogenic differentiation of stem cells. Nanoscale. https://doi.org/10.1039/d2nr03167a
64. Guo W, Liu C, Zhao F, Sun X, Yang Z, Chen T, Chen X, Qiu L, Hu X, Peng H (2012) A novel electromechanical actuation mechanism of a carbon nanotube fiber. Adv Mater 24:5379–5384. https://doi.org/10.1002/adma.201201845
65. Maziz A, Concas A, Khaldi A, Stålhand J, Persson NK, Jager EWH (2017) Knitting and weaving artificial muscles. Sci Adv 3:1–12. https://doi.org/10.1126/sciadv.1600327
66. Park J, Yoo JW, Seo HW, Lee Y (2017) Electrically controllable twisted-coiled artificial muscle actuators using surface-modified polyester fibers. Smart Mater Struct 26. https://doi.org/10.1088/1361-665X/aa5323
67. Chen P, Xu Y, He S, Sun X, Pan S, Deng J, Chen D, Peng H (2015) Hierarchically arranged helical fibre actuators driven by solvents and vapours. Nat Nanotechnol 10:1077–1083. https://doi.org/10.1038/nnano.2015.198
68. Mu J, de Andrade MJ, Fang S, Wang X, Gao E, Li N, Kim SH, Wang H, Hou C, Zhang Q, Zhu M, Qian D, Lu H, Kongahage D, Talebian S, Foroughi J, Spinks G, Kim H, Ware TH, Sim HJ, Lee DY, Jang Y, Kim SJ, Baughman RH (2019) Sheath-run artificial muscles. Science 155:150–155. https://doi.org/10.1126/science.aaw2403

69. Zhang Y, Pan C, Liu P, Peng L, Liu Z, Li Y, Wang Q, Wu T, Li Z, Majidi C, Jiang L (2023) Coaxially printed magnetic mechanical electrical hybrid structures with actuation and sensing functionalities. Nat Commun 14:1–15. https://doi.org/10.1038/s41467-023-40109-z
70. Kim Y, Parada GA, Liu S, Zhao X (2019) Ferromagnetic soft continuum robots. Sci Robot 4:1–15. https://doi.org/10.1126/SCIROBOTICS.AAX7329
71. Shi HTH, Pan Y, Xu L, Feng X, Wang W, Potluri P, Hu L, Hasan T, Huang YYS (2023) Sustainable electronic textiles towards scalable commercialization. Nat Mater 22. https://doi.org/10.1038/s41563-023-01615-z
72. Ovejero JG, Gallo-Cordova A, Roca AG, Morales MP, Veintemillas-Verdaguer S (2021) Reproducibility and scalability of magnetic nanoheater synthesis. Nanomaterials 11. https://doi.org/10.3390/nano11082059
73. Roca AG, Veintemillas-verdaguer S, Port M, Robic C, Serna CJ, Morales MP (2009) Effect of nanoparticle and aggregate size on the relaxometric properties of MR contrast agents based on high quality magnetite nanoparticles. J Phys Chem B 113:7033–7039. https://doi.org/10.1021/jp807820s

Supplementary information

High-performance magnetic artificial silk fibers produced by a scalable and eco-friendly production method

Gabriele Greco[1,&*] & Benjamin Schmuck[1,2,&], Lucia Del Bianco[3], Federico Spizzo[3], Luca Fambri[4], Nicola Maria Pugno[5,6], Sabino Veintemillas-Verdaguer[7], Maria Puerto Morales[7], Anna Rising[1,2*]

[1] Department of Animal Biosciences, Swedish University of Agricultural Sciences, Box 7011, Uppsala 75007, Sweden

[2] Department of Biosciences and Nutrition, Karolinska Institutet, Neo, 14183 Huddinge, Sweden

[3] Department of Physics and Earth Science, University of Ferrara, Via G. Saragat 1, 44122 Ferrara, Italy

[4] Department of Industrial Engineering and INSTM Research Unit, University of Trento, via Sommarive 9, 38123 Trento, Italy

[5] Laboratory for Bioinspired, Bionic, Nano, Meta Materials & Mechanics, Department of Civil, Environmental and Mechanical Engineering, University of Trento, Via Mesiano 77, 38123 Trento, Italy

[6] School of Engineering and Materials Science, Queen Mary University of London, UK, Mile End Road, London E1 4NS, UK

[7] Instituto de Ciencia de Materiales de Madrid, ICMM/CSIC, Sor Juana Inés de la Cruz 3, 28049 Madrid, Spain

[&] these authors contributed equally

*Corresponding authors: gabriele.greco@slu.se; anna.rising@slu.se;

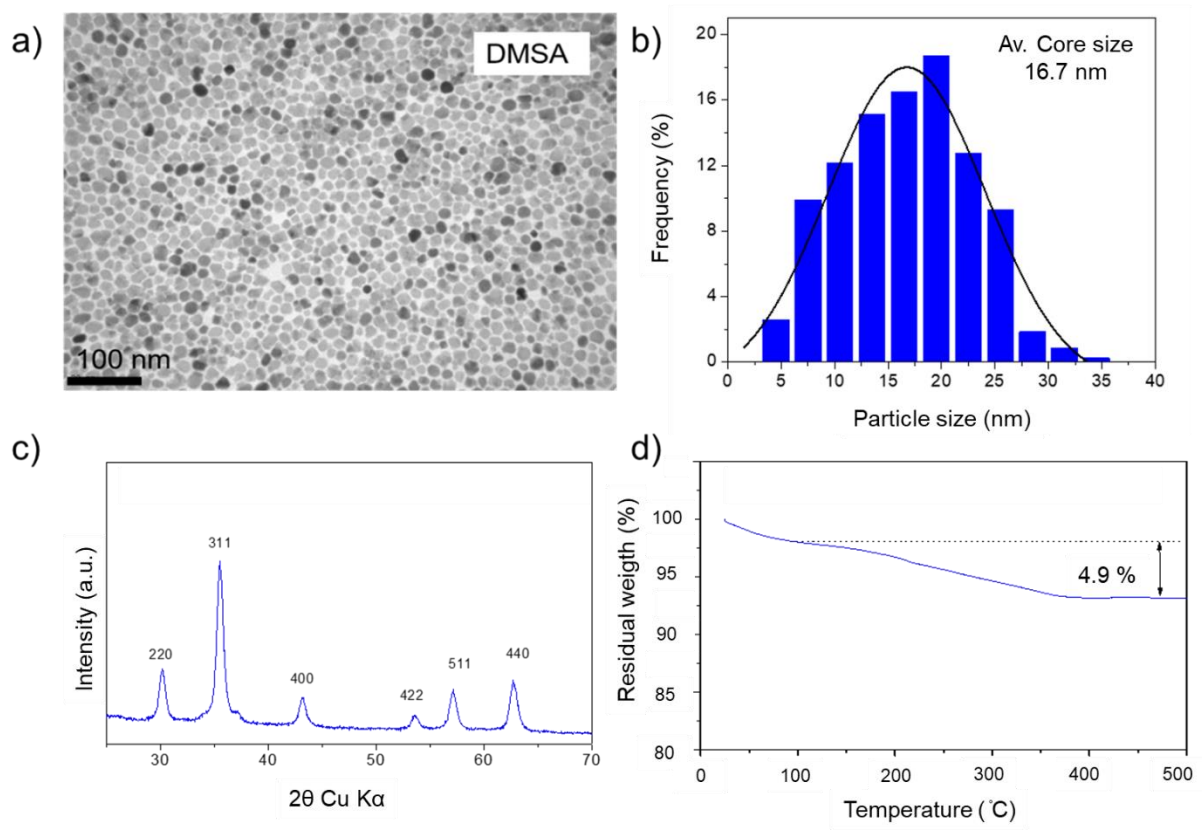

Figure S1: a) TEM image of the DMSA-coated magnetite nanoparticles, b) nanoparticle core size distribution, obtained by measuring about 800 particles, c) X-ray diffraction and d) thermogravimetric analysis.

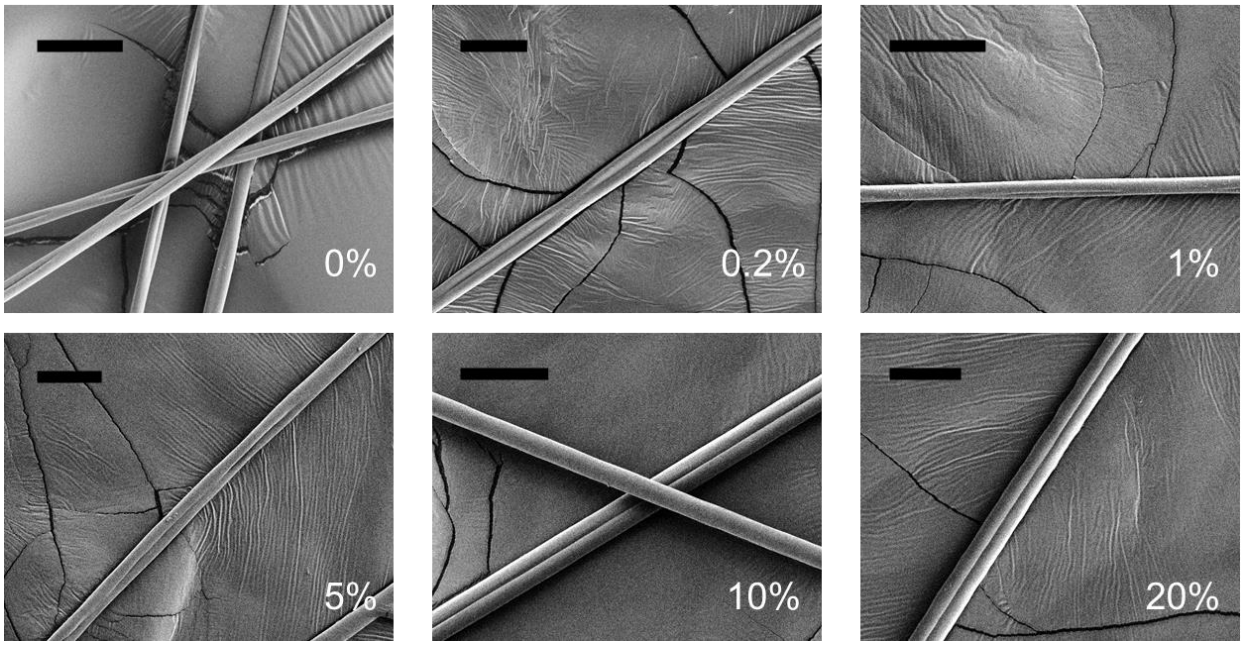

Figure S2: SEM images of the artificial magnetic spider silk fibers with different nominal w/w magnetite concentrations. Scale bars are 20 µm.

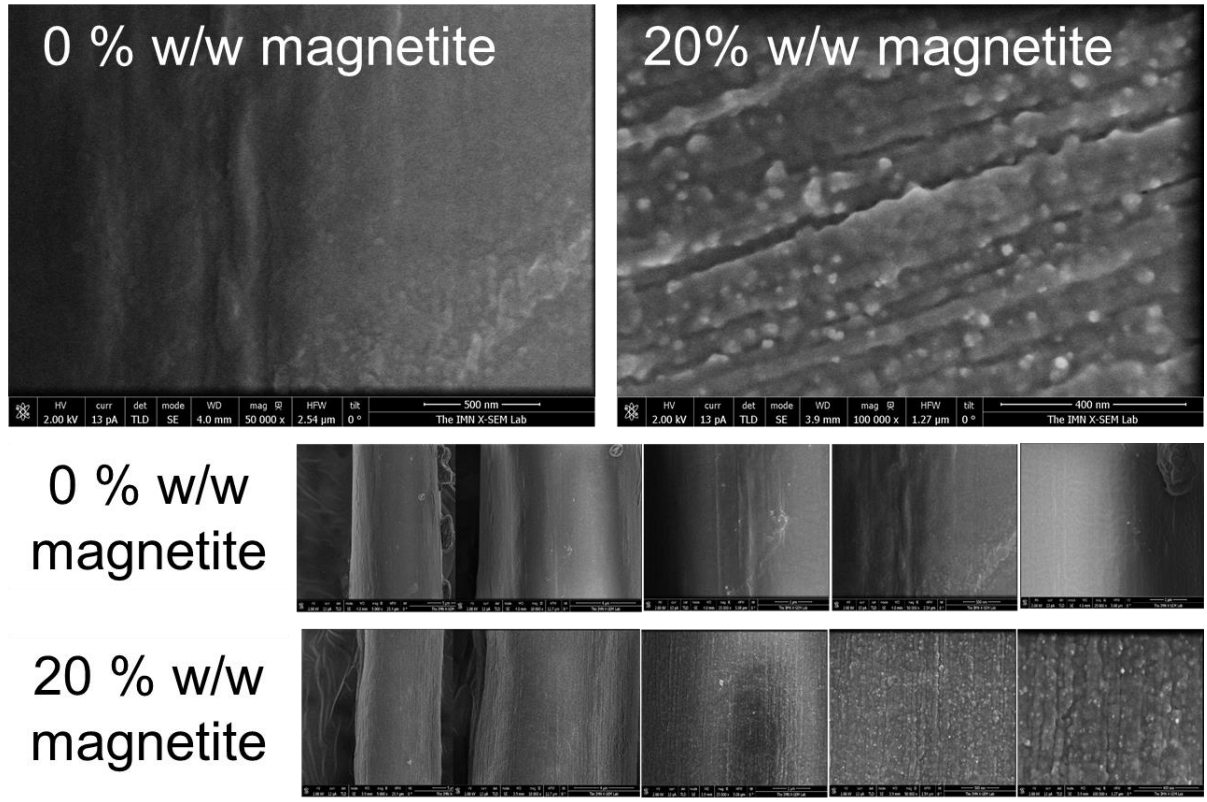

Figure S3: Representative high magnification SEM images of the NT2RepCT fibers (i.e., fibers containing no nanoparticles) and 20% w/w (nominal) of magnetite, which indicates homogeneous dispersion of the nanoparticles.

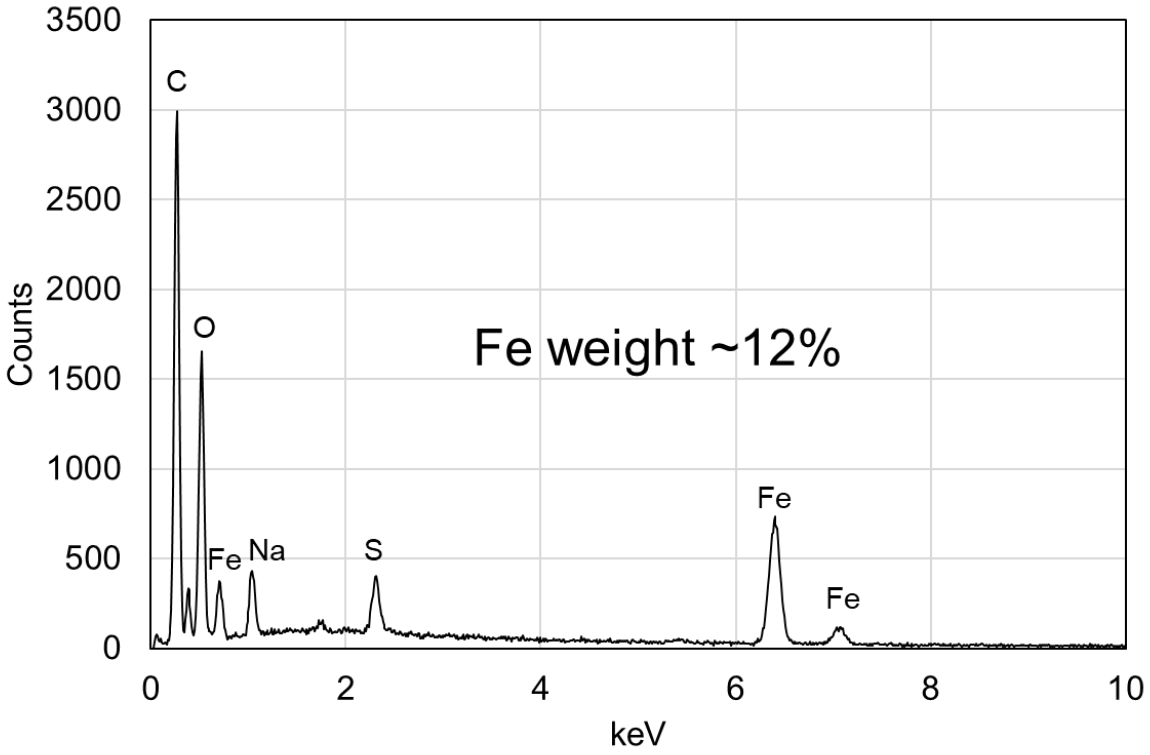

Figure S4: EDX spectra of the fibers having a 20% w/w nominal concentration of magnetite. According to the spectra, these fibers contain 12% w/w Fe, which corresponds to ~17% w/w magnetite.

Supplementary section S1: Magnetic properties of the fibers

For brevity, in this section and in Table S3, the composite fibers have been labeled as DX, where D stands for DMSA and X is a number referring to the nominal magnetite concentration. Magnetic loops, i.e. curves of magnetization M vs. magnetic field H, were measured on the whole set of composite fibers and on the nanoparticles alone by SQUID magnetometer, at T = 5 K and 300 K. For the nanoparticles alone (Fig. S5), the magnetization at H = 4×10^3 kA/m (taken as the saturation magnetization M_S) was corrected for the presence of the non-magnetic DMSA coating (~ 5 % w/w) in order to estimate the M_S of the magnetite phase alone. Hence, the obtained values were $M_S = (71.3 \pm 0.7)$ Am^2/kg at 5 K and $M_S = (62.8 \pm 0.6)$ Am^2/kg at 300 K.

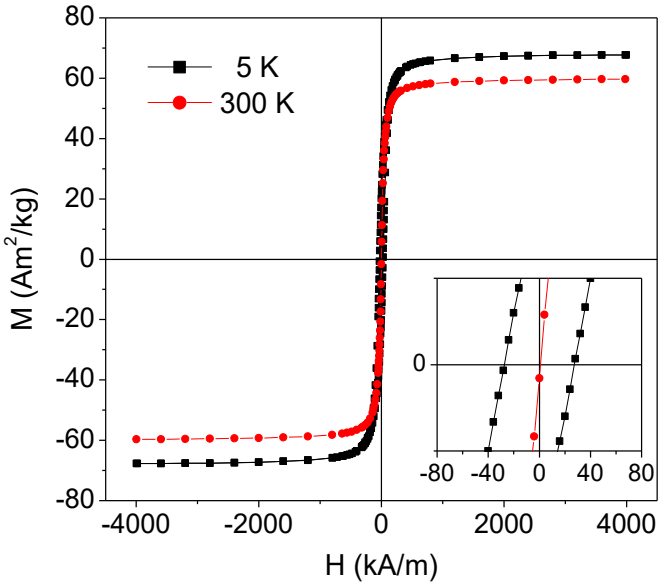

Figure S5: Magnetic loops measured at T = 5 K and 300 K on the DMSA-coated nanoparticles (i.e. the nanoparticles alone); the inset is a close-up of the central region of the loops.

The loops measured on the fiber samples at T = 5 K and 300 K are shown in Fig. S6 and Fig. 3, respectively. The values of saturation magnetization M_S at the two temperatures are reported in Table S3 together with the weight fractions of magnetite in the fibers (calculated by comparing the values of M_S to that obtained for the magnetite in the nanoparticles alone). The estimated concentrations are in good agreement with the nominal ones.

At T = 5 K, the coercivity H_C of samples D02, D1, and D5 is in the 27.1 ÷ 27.8 kA/m range, i.e. equal within the experimental errors; H_C for D10 and D20 is slightly lower, 25.5 ÷ 25.7 kA/m. At T = 300 K, no magnetic hysteresis is observed either in the nanoparticles alone or in the fiber samples, i.e. H_C and the remanent magnetization are null (Fig. 3a). This is consistent with a superparamagnetic behavior of the magnetic moments of the nanoparticles, in the adopted experimental conditions. In fact, it is known that the magnetic moment of an isolated single-domain nanoparticle can undergo magnetic relaxation, possibly culminating in the superparamagnetic behavior when the thermal energy is comparable to the anisotropy energy barrier for its reversal[1]. The blocking temperature T_B, above which a magnetic nanoparticle enters the superparamagnetic regime, is given by the relation:

$$T_B = KV/[k_B \ln(t_m f_0)] \qquad (1)$$

where KV is the anisotropy energy barrier (K magnetic anisotropy coefficient, V volume of the nanoparticle), k_B is the Boltzmann constant, t_m is the measuring time characteristic of the adopted analysis technique and f_0 is a frequency factor[1]. For SQUID measurements, t_m and f_0 are usually taken equal to 100 s and 10^9 s^{-1}, respectively, and therefore $\ln(t_m f_0) \sim 25$[2,3].

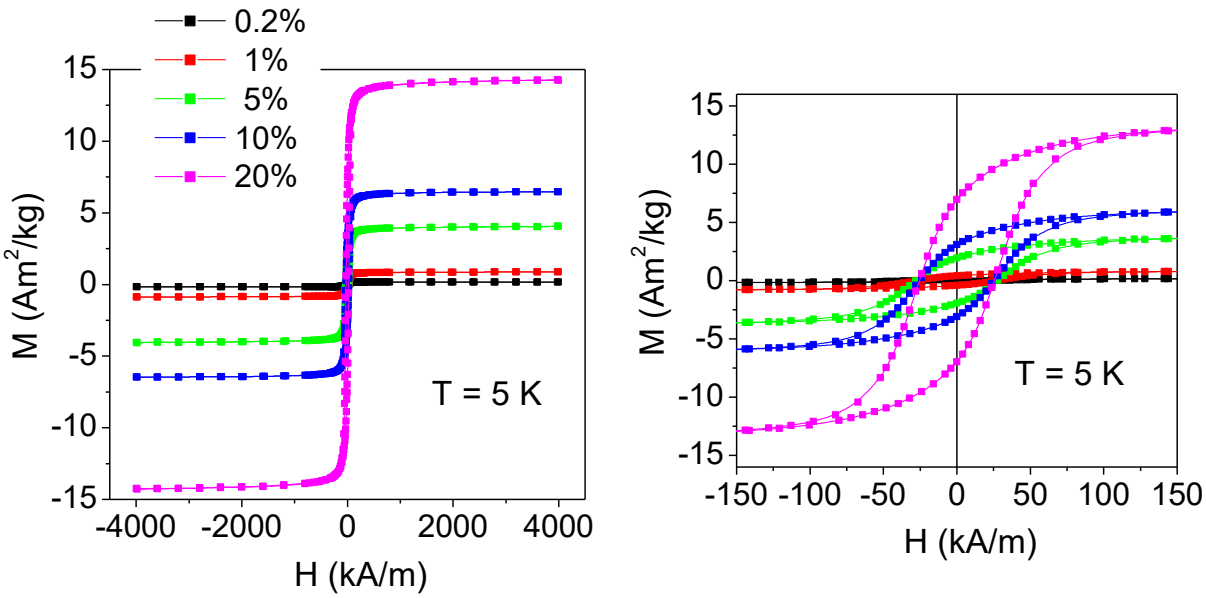

Figure S6: Left: Magnetic hysteresis loops measured at T = 5 K on the set of composite fibers, corrected for the magnetic signal from the spidroin matrix. Right: close-up of the central region of the loops. Different colors indicate different nominal w/w magnetite concentrations.

Information on the relaxing behavior of the nanoparticles in the fibers was gained through the analysis of the thermoremanent magnetization (TRM) vs. T and corresponding temperature derivatives curve, i.e. [-d(TRM)/dT] vs. T[1,4,5]. The latter provides a figure of the distribution of anisotropy energy barriers associated with the assembly of nanoparticles embedded in the fibers and, based on equation (1), also of the distribution of blocking temperatures T_B. The results are shown in Fig. 3b,c. In all samples, TRM goes to zero with increasing temperature, confirming the progressive entrance of the nanoparticles into the superparamagnetic regime. For samples D02, D1, and D5, the derivative curves exhibit a similar profile, consistent with a quite narrow anisotropy energy barrier distribution with a peak temperature of 70-80 K (Fig. 3c), which can be taken as a mean blocking temperature $\langle T_B \rangle$. From equation (1), considering that the mean size of the magnetic core of the nanoparticles is ~ 17 nm (Table S1) and setting K equal to that of bulk magnetite (1.0×10^4 J/m^3), a value $\langle T_B \rangle$ ~ 72 K is obtained. This good agreement between the measured and predicted average blocking temperature indicates that, in the samples with low magnetic load, the nanoparticles are very homogeneously dispersed and are far apart from each other, so that dipolar magnetic interactions are not strong enough to affect their relaxing behavior. A slightly different situation is observed for samples D10 and D20, which show broader distributions reaching a maximum at ~100 K and ~110 K, respectively (Fig. 3c). The shift to a higher temperature of the anisotropy energy barrier distribution is to be ascribed to the existence of non-negligible interparticle dipolar interactions[1–3,6–9]. Since dipolar interactions are demagnetizing in nature, their presence can also account for the smaller H_C of D10 and D20 at T = 5 K, compared to the other samples (Table S3). To evaluate to what extent the magnetic behavior of the nanoparticles is affected by dipolar interactions, a mean effective magnetic anisotropy $\langle K_{eff} \rangle$ can be calculated from equation (1), taking the peak temperature of the distribution as the $\langle T_B \rangle$ value. The obtained results are $\langle K_{eff} \rangle = 1.4\times10^4$ J/m^3 for D10 and $\langle K_{eff} \rangle = 1.5\times10^4$ J/m^3 for D20, significantly larger than that of bulk magnetite. However, they are very similar, which is unexpected if one considers that, with doubling the fraction of nanoparticles, the interparticle distance should reduce and therefore the strength of dipolar interactions should increase. Indeed, these findings reveal that a less homogeneous spatial distribution of the nanoparticles is attained in D10 and D20, compared to the fibers with lower magnetic load. The existence of regions with different local

concentrations of nanoparticles in the spidroin matrix can explain the observed broadening of the distribution of anisotropy energy barriers (i.e., of effective barriers). On the other hand, an inhomogeneous arrangement of the nanoparticles may also imply that on average the interparticle distance is similar in the two samples, thus accounting for the close values of $\langle K_{eff} \rangle$.

This description is supported by the analysis of the ΔM plots, which is a powerful method to gain information on the nature of magnetic interactions in nanoparticle assemblies [2,3,5]. In particular, a negative ΔM plot indicates the existence of dipolar interactions and the absolute peak value of ΔM provides qualitative information on their strength. Hence, the ΔM plots collected on the composite fibers at T = 20 K, shown in Fig. S7, confirm the existence of dipolar interactions whose strength tends to increase with increasing the nanoparticle load, but is substantially similar in samples D10 and D20.

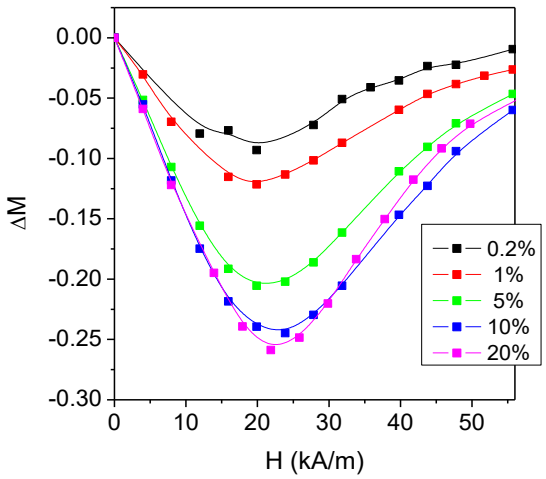

Figure S7: ΔM-plots at T = 20 K for the composite fibers. Different colors indicate different nominal w/w magnetite concentrations. The ΔM parameter is calculated as ΔM(H) = DCD(H)-[1- 2IRM(H)].

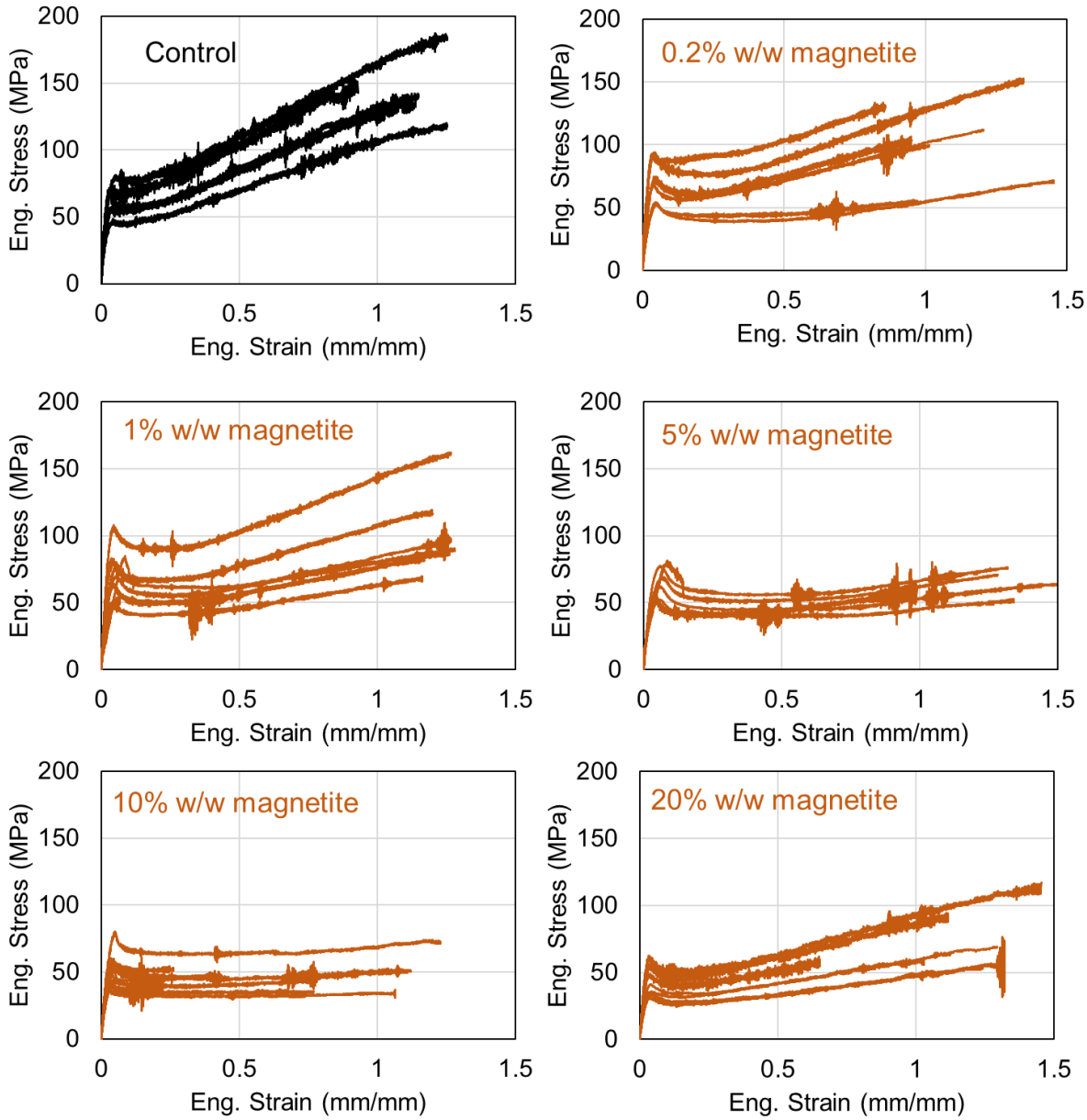

Figure S8: Representative stress-strain curves of composite fibers with different levels of nominal w/w magnetite concentrations.

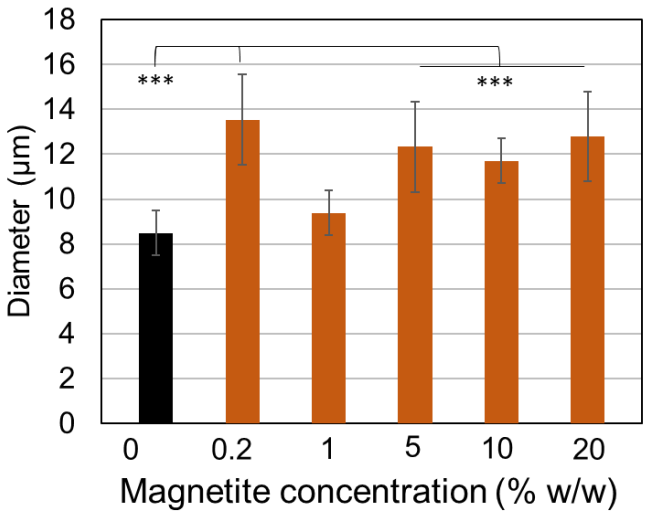

*Figure S9: Diameters of the magnetic artificial silk fibers vs. the nominal magnetite concentration (w/w). * Indicate p-value <0.05, ** p-value <0.01, and *** p-value < 0.001.*

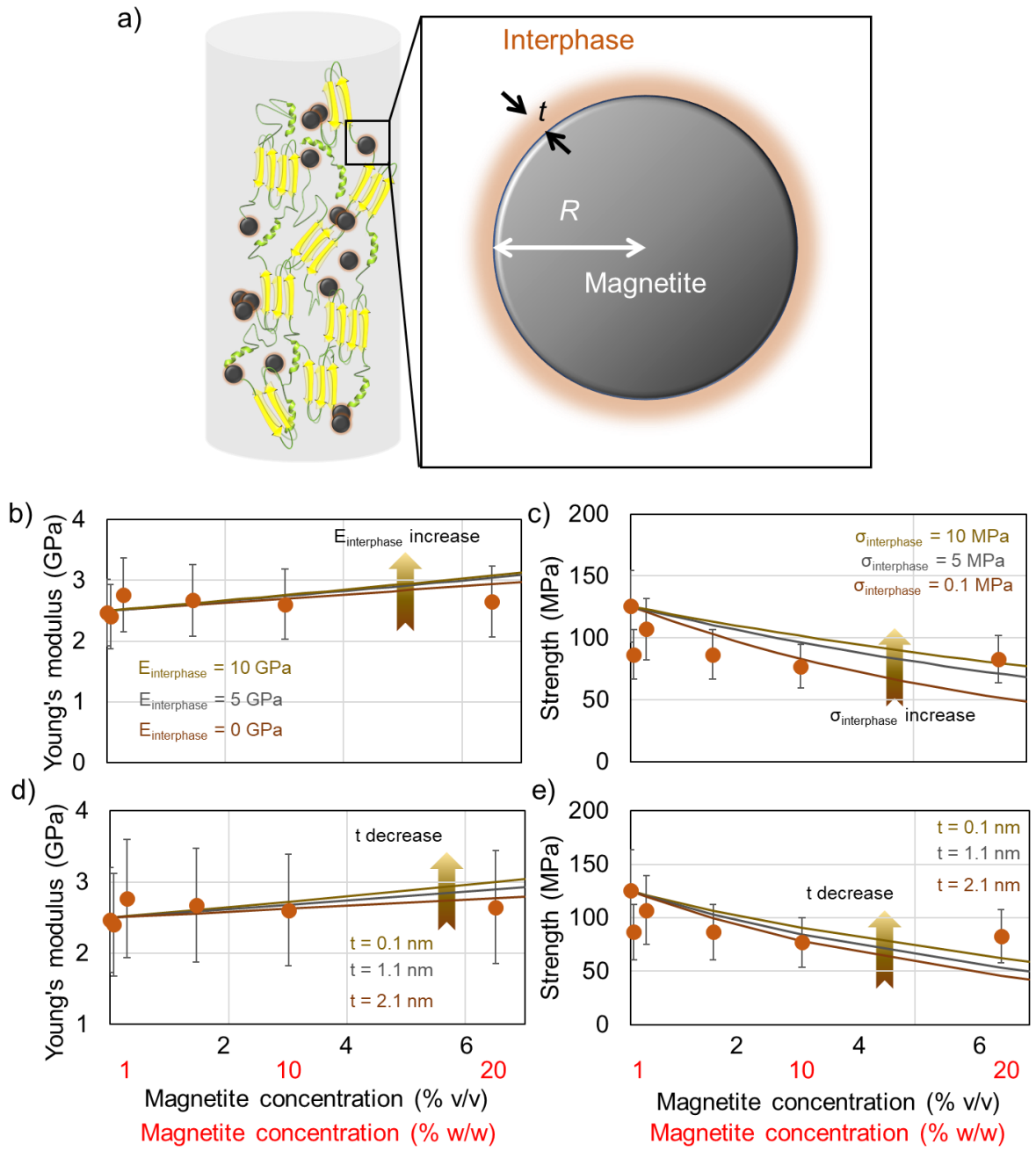

Figure S10: a) Schematic of the model used to interpret the impact of the mechanical properties of the interphase on the mechanical properties of the composite fibers. The relative dimensions between the nanoparticles and the secondary structure is only for representation purposes. Plot of the experimental values of the mechanical properties and the theoretical lines obtained from the model, and in particular for equation b) 2, c) 3, d), 4, and e) 5. To plot the model, the protein matrix (NT2RepCT) has been considered with a strength of 125 MPa and a Young's modulus of 2.5 GPa. For panel d), a value of $E_{interphase}$ = 0 GPa was used. For panel e), a value of $\sigma_{interphase}$ = 0.1 MPa was used.

Supplementary section S2: Analytical model of the composite

The analytical model to explain the effect of the nanoparticle volumetric concentration on the mechanical properties of the magnetic artificial silk fiber was developed by Zare[10], which is an extension of Maxwell[11] and Pukànsky[12] theories for composites (for Young's modulus E and strength σ_C of the composite respectively). Fig. S10a depicts the geometry of the system: thickness of the interphase (t), and radius of the nanoparticle (R). In this model, we assumed that the nanoparticles are homogeneously dispersed in the matrix, which agrees

with the experimental findings. Furthermore, we consider the properties of the interphase as a combination of the DMSA coating mechanical properties, the interface interactions between the magnetite and the DMSA, and the interface interactions between the DMSA and the protein.

In the model is added a third phase (the interphase between the filler and the matrix). The equations for Young's modulus of the fibrous composite and the strength are

$$E = E_m \frac{1 + \frac{2\phi_f\left(E_f/E_m - 1\right)}{E_f/E_m + 2} + \frac{2\phi_i(E_i/E_m - 1)}{E_i/E_m + 2}}{1 - \frac{\phi_f\left(E_f/E_m - 1\right)}{E_f/E_m + 2} - \frac{\phi_i(E_i/E_m - 1)}{E_i/E_m + 2}} \quad (2)$$

$$\sigma_R = \frac{\sigma_c}{\sigma_m} = \frac{1 - \phi_f}{1 + 2.5\phi_f} \exp\left[\left(\phi_f + 3\phi_f\left(\frac{\phi_i}{\phi_f} + 1\right)^{\frac{1}{3}} - 3\phi_f\right)\ln\left(\frac{\sigma_i}{\sigma_m}\right)\right] \quad (3)$$

where E_m, E_i, and E_f are the Young's moduli of the matrix, the interphase and the filler, ϕ_f and ϕ_i are the volumetric fractions of the filler and the interphase respectively, and finally σ_R, σ_c, σ_m, and σ_i are the relative strength of the composite, the strength of the composite, the matrix, and the interphase respectively.

Equations 2 and 3 can be also written in terms of *t* and *R*. They become

$$E = E_m \frac{1 + \frac{2\phi_f\left(E_f/E_m - 1\right)}{E_f/E_m + 2} + \frac{2\phi_f\left[\left(\frac{R+t}{R}\right)^3 - 1\right](E_i/E_m - 1)}{E_i/E_m + 2}}{1 - \frac{\phi_f\left(E_f/E_m - 1\right)}{E_f/E_m + 2} - \frac{\phi_f\left[\left(\frac{R+t}{R}\right)^3 - 1\right](E_i/E_m - 1)}{E_i/E_m + 2}} \quad (4)$$

$$\sigma_R = \frac{\sigma_c}{\sigma_m} = \frac{1 - \phi_f}{1 + 2.5\phi_f} \exp\left[\left(\phi_f + 3\phi_f\left(\frac{\phi_f\left[\left(\frac{R+t}{R}\right)^3 - 1\right]}{\phi_f} + 1\right)^{\frac{1}{3}} - 3\phi_f\right)\ln\left(\frac{\sigma_i}{\sigma_m}\right)\right] \quad (5)$$

To plot equations 2-5, we calculated the volume fractions of magnetite (Table S4) considering the mass density values of bulk magnetite (~ 5 x 10^3 kg/m^3), DMSA (~ 1.6 x 10^3 kg/m^3, see ref[13]), and artificial spider silk fibers (measured value [1.41 ± 0.09] x 10^3 kg/m^3, Fig. S11). The volumetric fraction of the interphase is here assumed to be the volumetric fraction of the DMSA coating. Furthermore, we also considered that the DMSA coating constitutes ~5% w/w of the nanoparticle (Fig. S1). This data is important to estimate the thickness of the interphase, i.e., the thickness of the DMSA coating, which can be obtained by geometrical considerations and turns out to be ~ 0.4 nm. To plot the graph, we used values between 0.1-2.1 nm to show a broader range. Furthermore, the parameters that can be extrapolated from experimental data are the radius of the magnetite nanoparticle (~9 nm including DMSA coating), the strength and Young's modulus of the matrix (125 MPa and 2.5 GPa from the mechanical data obtained with tensile tests) and Young's modulus of the magnetite (300 GPa from literature[14]). The unknown parameters are the strength and Young's modulus of the interphase. We thus used different numbers to show their effect on the mechanical properties of the composite fiber. Once these parameters are defined, the

strength and Young's modulus of the composite fiber can be plotted vs. volumetric magnetite fraction (Fig. S10). From this model and in the conditions that we explored to fit the graphs, it is possible to state that, to have a significant reinforcement, the strength and Young's modulus of the interphase have to be much higher compared to the matrix. In particular, to produce a significant increase of Young's modulus at low magnetite concentrations the interphase must have a Young' modulus >>10 GPa (Fig. S10b). To lead to an increase in strength, the strength of the interphase must be at least >125 MPa (equation 3, Fig. S10c). Moreover, the thickness of the DMSA coating seems to have a minor effect in the explored range and at volumetric magnetite concentrations lower than 20% (Fig. S10d, e). This also is consistent with the estimation of the DMSA coating thickness (0.4 nm).

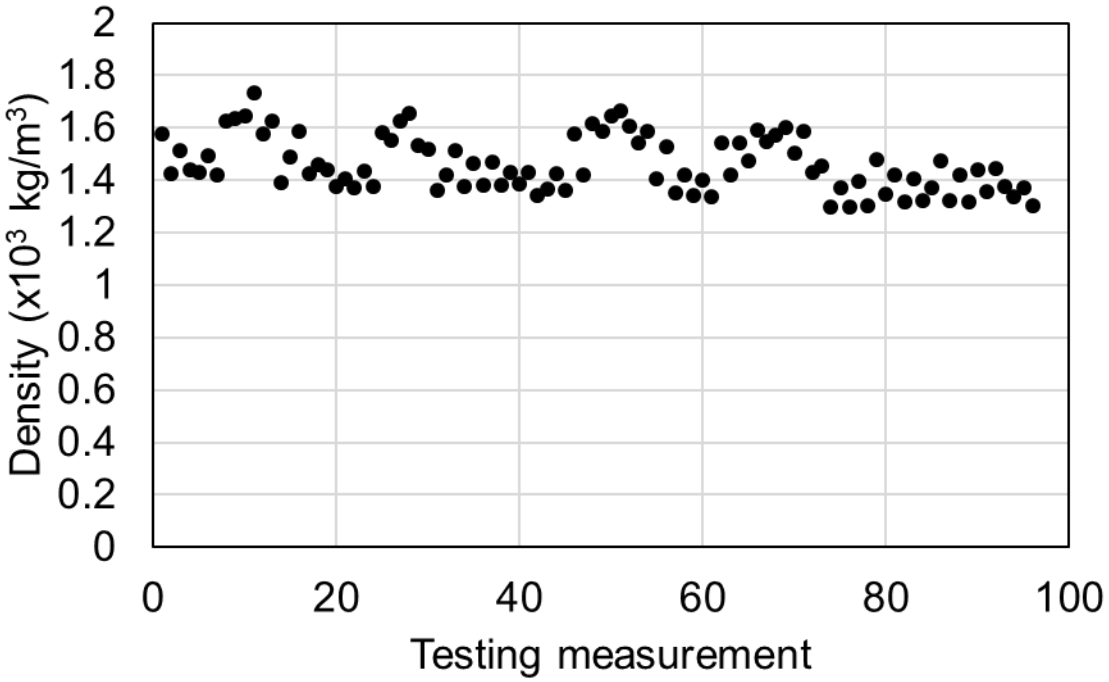

Figure S11: Density measurements of about 35 mg of NT2RepCT fibers carried out in a pycnometer at 23.0°C. The obtained value of density is (1.41 ± 0.09) x 10^3 kg/m^3.

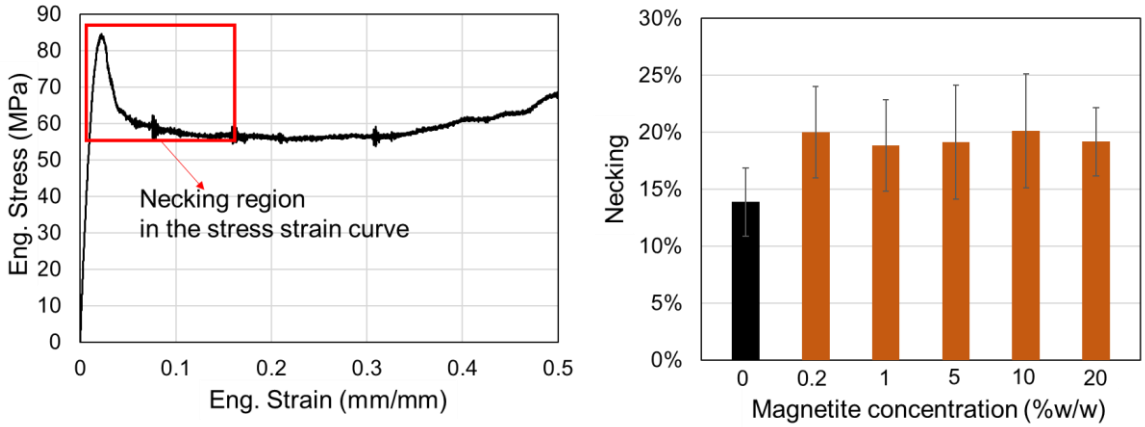

Figure S12: Representative necking of a representative stress strain curve of a silk fiber and necking values vs. the nominal magnetite concentration (w/w).

Supplementary section S3: Surface Plasmon Resonance (SPR)-assay

The basic principle of an SPR assay is that the reflection angle of a light beam away from a gold surface is influenced by the refractive index of the surface, which is directly correlated with the weight of the molecules on a gold chip. Thus, the presence of additional weight on a gold surface can be detected label-free, by directing a polarized light beam with a single wavelength onto the bottom of the gold surface.

Since immobilization of the ligand, NT2RepCT, on the gold surface of the sensor chip increased the weight, an increase in the relative response was detected (Fig. S13 A). In fact, an immobilization level of more than 3000 RU was achieved, which is close to the upper limit of this chip, also indicated by the fact that a substantial amount of NT2RepCT leaks from the surface after the injection event (indicated by an arrow). To detect the presence or absence of an interaction between the spidroin and the magnetite nanoparticles, the nanoparticles are subsequently injected over the same surface, which is available to be captured by the NT2RepCT. If both entities interact, this will add an additional weight to the gold surface, which should increase the response relative to a reference surface where no ligand is bound. The sensorgram shown in Fig. S13 is reference subtracted (on the reference surface NT2RepCT was not immobilized) and shows the point where the analyte (the nanoparticles) was injected (Fig. S13B). Even though a very high immobilization level of NT2RepCT and a high concentration of nanoparticles (4.6 µg/mL) was used in this particular assay, the instrument did not detect any additional weight on the sensor surface compared to the reference and the blank sample. This indicates that NT2RepCT and the nanoparticles do not interact or the interaction is very weak.

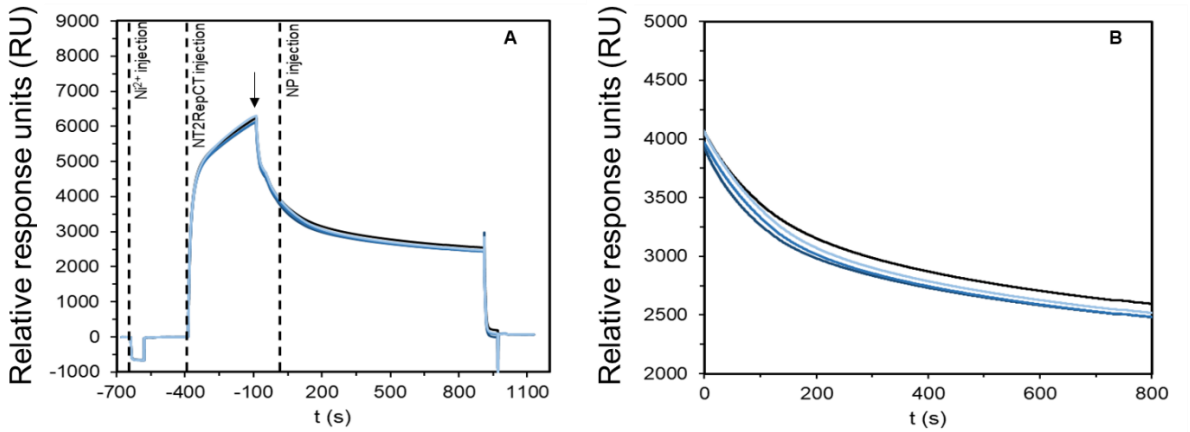

Figure S13: Sensorgram obtained with an SPR-assay to detect if there is an interaction between the DMSA-coated magnetite nanoparticles and NT2RepCT. (A) Complete sensorgram featuring the events of nickel binding to an NTA-chip, followed by washing and injection of the ligand (NT2RepCT), and finally injection of the nanoparticles. These events are indicated by dashed lines. (B) Zoom in on the sensorgram shown in A. Injection of Analyte (DMSA coated nanoparticles) onto NT2RepCT immobilized on a gold chip in an SPR-assay. The injection event of 4.6 µg/ml (dark blue), 0.46 µg/ml (blue), 0.046 µg/ml (light blue), and 0 nM (black) magnetite starts at t=0s.

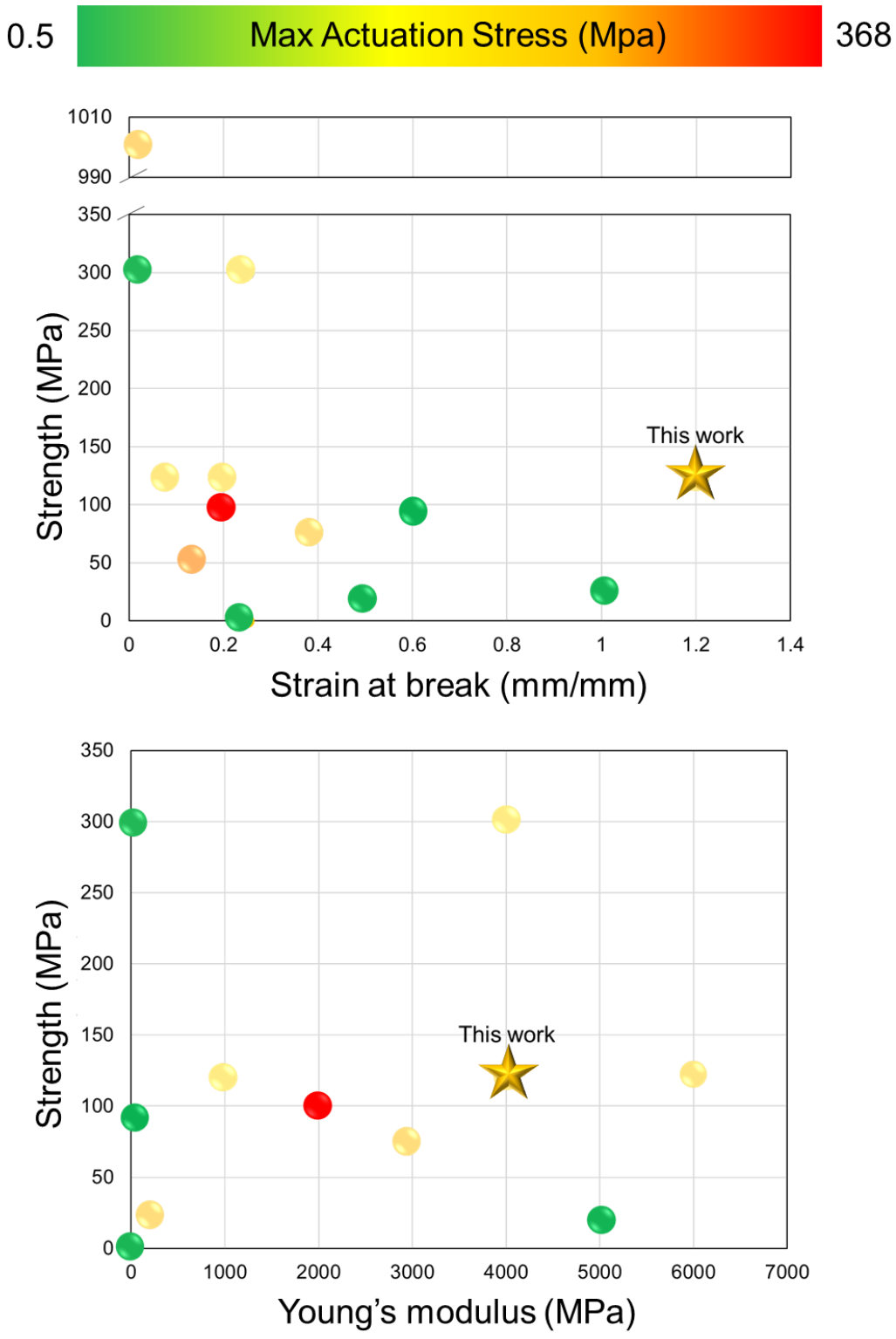

Figure S14: Mechanical properties plotted vs. the maximal actuation stress generated by standard fibrous materials, the data were obtained from[15–28].

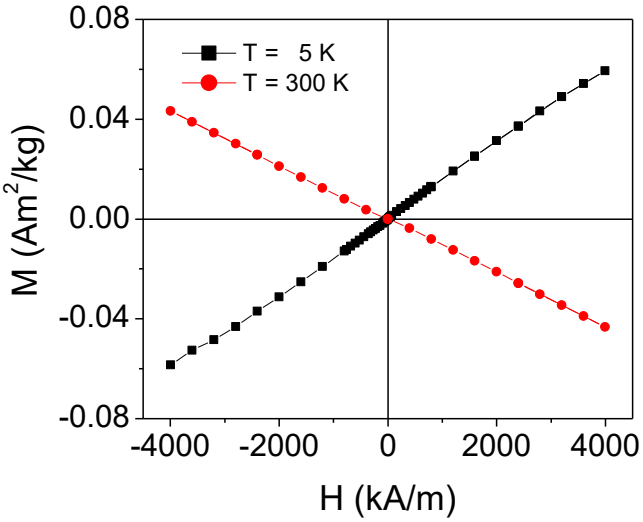

Figure S15: Curves of Magnetization M vs. magnetic field H measured on the NT2RepCT fibers (i.e., fibers containing no nanoparticles) at the indicated temperatures.

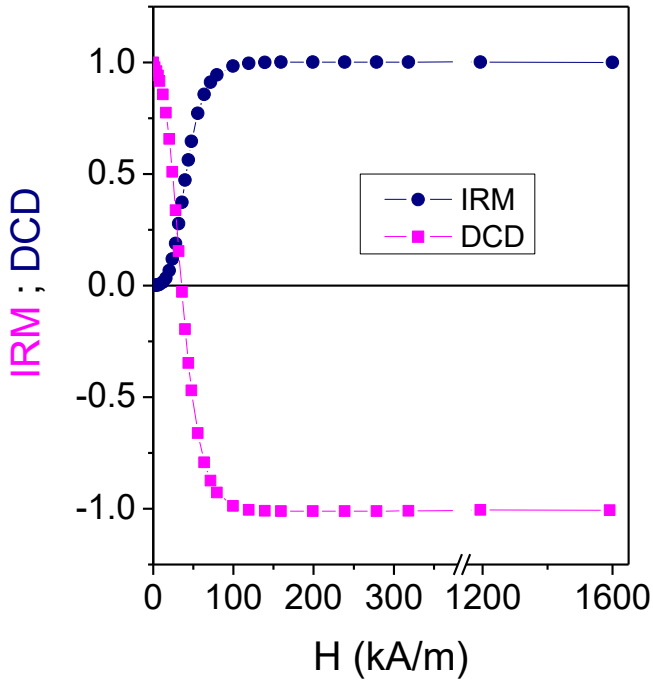

Figure S16: Isothermal remanent magnetization (IRM) and dc demagnetization remanence (DCD) curves, measured at T = 20 K on fibers with 20% w/w magnetite.

Table S1: Physical properties of the DMSA-coated magnetite nanoparticles.

Core	Coating	Average nanoparticle core size TEM (nm)	Crystal size X-ray (nm)	Hydrodynamic size (nm)	Z-Potential (mV)
Fe_3O_4	Dimercaptosuccinic acid	16.7 (σ=0.16)	~13	74(PDI= 0.23)	-27

Table S2: The nanomaterial concentrations that were used to achieve the optimal mechanical properties of different silk-nanomaterials composites.

Type of nanomaterial	***Concentration to obtain maximum strain at break or strength (w/w)***	***Max concentration explored (w/w)***	***Reference***
Single-walled carbon nanotubes	*1%*	*2%*	[29]
Multiwalled carbon nanotubes	*1%*	*1.5%*	[30]
Carbon nanotubes	*<0.5%*	*<0.5%*	[31]
Carbon nanotubes	*0.2%*	*1%*	[32]
Single-walled carbon nanotubes	*0.2%*	*1%*	[33]
Graphene oxide	*0.1%*	*0.2%*	[34]
Magnetite nanoparticles	*0.2-1%*	*20%*	*This study*

Table S3: Magnetization and magnetic coercivity of the artificial silk fibers and estimated w/w magnetite concentrations.

Sample	**Nominal magnetite fraction (w/w %)**	**M_S at T = 5 K (Am^2/kg) ± 3%**	**M_S at T = 300 K (Am^2/kg) ± 3%**	**H_C at T = 5K (kA/m) ± 0.4**	**Estimated magnetite fraction (w/w %) ± 5%**
D02	0.2	0.172	0.148	27.1	0.24
D1	1	0.88	0.74	27.1	1.18
D5	5	4.1	3.50	27.8	5.6
D10	10	6.5	5.7	25.5	9.1
D20	20	14.3	12.5	25.7	20

Table S4: Estimated magnetite volume fractions in the magnetic artificial silk fibers.

Nominal magnetite fraction (w/w %)	**Estimated magnetite fraction (% volume) ± 10%**
0.2	0.07
1	0.33
5	1.63
10	2.7
20	6.5

Additional References:

[1] J.L. Dormann, D. Fiorani, E. Tronc, Magnetic Relaxation in Fine-Particle Systems, in: Adv. Chem. Phys. Vol. XCVIII, John Wiley & Sons, Inc.: New York, USA, 2007: pp. 283–494. https://doi.org/10.1002/9780470141571.ch4.

[2] L. Del Bianco, F. Spizzo, G. Barucca, M.R. Ruggiero, S. Geninatti Crich, M. Forzan, E. Sieni, P. Sgarbossa, Mechanism of magnetic heating in Mn-doped magnetite nanoparticles and the role of intertwined structural and magnetic properties, Nanoscale. 11 (2019) 10896–10910. https://doi.org/10.1039/c9nr03131f.

[3] M. Blanco-Mantecón, K. O'Grady, Interaction and size effects in magnetic nanoparticles, J. Magn. Magn. Mater. 296 (2006) 124–133. https://doi.org/10.1016/j.jmmm.2004.11.580.

[4] J.G. Ovejero, F. Spizzo, M.P. Morales, L. Del Bianco, Mixing iron oxide nanoparticles with different shape

and size for tunable magneto-heating performance, Nanoscale. 13 (2021) 5714–5729. https://doi.org/10.1039/d0nr09121a.
[5] K. O'Grady, R.W. Chantrell, Remanence Curves of Fine Particle Systems I: Experimental Studies, in: Magn. Prop. Fine Part., Elsevier, 1992: pp. 93–102. https://doi.org/10.1016/b978-0-444-89552-3.50017-7.
[6] G.F. Goya, T.S. Berquó, F.C. Fonseca, M.P. Morales, Static and dynamic magnetic properties of spherical magnetite nanoparticles, J. Appl. Phys. 94 (2003) 3520–3528. https://doi.org/10.1063/1.1599959.
[7] M. El-Hilo, K. O'Grady, R.W. Chantrell, Susceptibility phenomena in a fine particle system. I. Concentration dependence of the peak, J. Magn. Magn. Mater. 114 (1992) 295–306. https://doi.org/10.1016/0304-8853(92)90272-P.
[8] C. Binns, M.J. Maher, Q.A. Pankhurst, D. Kechrakos, K.N. Trohidou, Magnetic behavior of nanostructured films assembled from preformed Fe clusters embedded in Ag, Phys. Rev. B - Condens. Matter Mater. Phys. 66 (2002) 1–12. https://doi.org/10.1103/PhysRevB.66.184413.
[9] J.G. Ovejero, F. Spizzo, M.P. Morales, L. Del Bianco, Nanoparticles for magnetic heating: When two (or more) is better than one, Materials (Basel). 14 (2021) 6416. https://doi.org/10.3390/ma14216416.
[10] Y. Zare, The roles of nanoparticles accumulation and interphase properties in properties of polymer particulate nanocomposites by a multi-step methodology, Compos. Part A Appl. Sci. Manuf. 91 (2016) 127–132. https://doi.org/10.1016/j.compositesa.2016.10.003.
[11] J.C. Maxwell, A Treatise on Electricity and Magnetism, Cambridge University Press, 1873. https://doi.org/10.1017/CBO9780511709333.
[12] B. Pukánszky, Influence of interface interaction on the ultimate tensile properties of polymer composites, Composites. 21 (1990) 255–262. https://doi.org/10.1016/0010-4361(90)90240-W.
[13] Chem-Search engine, (2023).
[14] D. Chicot, J. Mendoza, A. Zaoui, G. Louis, V. Lepingle, F. Roudet, J. Lesage, Mechanical properties of magnetite (Fe3O4), hematite (Fe2O3) and goethite (FeOOH) by instrumented indentation and molecular dynamics analysis, Mater. Chem. Phys. 129 (2011) 862–870. https://doi.org/10.1016/j.matchemphys.2011.05.056.
[15] J.A. Lee, Y.T. Kim, G.M. Spinks, D. Suh, X. Lepró, M.D. Lima, R.H. Baughman, S.J. Kim, All-solid-state carbon nanotube torsional and tensile artificial muscles, Nano Lett. 14 (2014) 2664–2669. https://doi.org/10.1021/nl500526r.
[16] W. Guo, C. Liu, F. Zhao, X. Sun, Z. Yang, T. Chen, X. Chen, L. Qiu, X. Hu, H. Peng, A novel electromechanical actuation mechanism of a carbon nanotube fiber, Adv. Mater. 24 (2012) 5379–5384. https://doi.org/10.1002/adma.201201845.
[17] J. Mu, M.J. de Andrade, S. Fang, X. Wang, E. Gao, N. Li, S.H. Kim, H. Wang, C. Hou, Q. Zhang, M. Zhu, D. Qian, H. Lu, D. Kongahage, S. Talebian, J. Foroughi, G. Spinks, H. Kim, T.H. Ware, H.J. Sim, D.Y. Lee, Y. Jang, S.J. Kim, R.H. Baughman, Sheath-run artificial muscles, Science (80-.). 155 (2019) 150–155. https://doi.org/10.1126/science.aaw2403.
[18] W. Wang, C. Xiang, Q. Liu, M. Li, W. Zhong, K. Yan, D. Wang, Natural alginate fiber-based actuator driven by water or moisture for energy harvesting and smart controller applications, J. Mater. Chem. A. 6 (2018) 22599–22608. https://doi.org/10.1039/c8ta08064j.
[19] D.W. Lee, S.H. Kim, M.E. Kozlov, X. Lepró, R.H. Baughman, S.J. Kim, Magnetic torsional actuation of carbon nanotube yarn artificial muscle, RSC Adv. 8 (2018) 17421–17425. https://doi.org/10.1039/c8ra01040d.
[20] Y. Kim, H. Yuk, R. Zhao, S.A. Chester, X. Zhao, Printing ferromagnetic domains for untethered fast-transforming soft materials, Nature. 558 (2018) 274–291. https://doi.org/10.1038/s41586-018-0185-0.
[21] A. Maziz, A. Concas, A. Khaldi, J. Stålhand, N.K. Persson, E.W.H. Jager, Knitting and weaving artificial muscles, Sci. Adv. 3 (2017) 1–12. https://doi.org/10.1126/sciadv.1600327.
[22] L. Ionov, G. Stoychev, D. Jehnichen, J.U. Sommer, Reversibly Actuating Solid Janus Polymeric Fibers, ACS Appl. Mater. Interfaces. 9 (2017) 4873–4881. https://doi.org/10.1021/acsami.6b13084.
[23] C.S. Haines, M.D. Lima, N. Li, G.M. Spinks, J. Foroughi, J.D.W. Madden, S.H. Kim, S. Fang, M.J. De Andrade, F. Göktepe, Ö. Göktepe, S.M. Mirvakili, S. Naficy, X. Lepró, J. Oh, M.E. Kozlov, S.J. Kim, X. Xu, B.J. Swedlove, G.G. Wallace, R.H. Baughman, Artificial muscles from fishing line and sewing thread, Science (80-.). 343 (2014) 868–872. https://doi.org/10.1126/science.1246906.
[24] J. Park, J.W. Yoo, H.W. Seo, Y. Lee, Electrically controllable twisted-coiled artificial muscle actuators using surface-modified polyester fibers, Smart Mater. Struct. 26 (2017). https://doi.org/10.1088/1361-665X/aa5323.
[25] M.D. Lima, N. Li, M.J. De Andrade, S. Fang, J. Oh, G.M. Spinks, M.E. Kozlov, C.S. Haines, D. Suh, J. Foroughi, S.J. Kim, Y. Chen, T. Ware, M.K. Shin, L.D. Machado, A.F. Fonseca, J.D.W. Madden, W.E. Voit, D.S. Galvão, R.H. Baughman, Electrically, chemically, and photonically powered torsional and tensile actuation of hybrid carbon nanotube yarn muscles, Science (80-.). 338 (2012) 928–932. https://doi.org/10.1126/science.1226762.
[26] M.O. Saed, C.P. Ambulo, H. Kim, R. De, V. Raval, K. Searles, D.A. Siddiqui, J.M.O. Cue, M.C. Stefan, M.R. Shankar, T.H. Ware, Molecularly-Engineered 4D-Printed Liquid Crystal Elastomer Actuators.pdf, Adv. Funct. Mater. 29 (2019). https://doi.org/10.1002/adfm.201806412.
[27] P. Chen, Y. Xu, S. He, X. Sun, S. Pan, J. Deng, D. Chen, H. Peng, Hierarchically arranged helical fibre actuators driven by solvents and vapours, Nat. Nanotechnol. 10 (2015) 1077–1083.

https://doi.org/10.1038/nnano.2015.198.
[28] T. Jia, Y. Wang, Y. Dou, Y. Li, M.J. de Andrade, R. Wang, S. Fang, J. Li, Z. Yu, R. Qiao, Z. Liu, Y. Cheng, Y. Su, M. Minary-Jolandan, R.H. Baughman, D. Qian, Z. Liu, Moisture Sensitive Smart Yarns and Textiles from Self-Balanced Silk Fiber Muscles.pdf, Adv. Funct. Mater. 29 (2019). https://doi.org/10.1002/adfm.201808241.
[29] J. Ayutsede, M. Gandhi, S. Sukigara, H. Ye, C. Hsu, Y. Gogotsi, F. Ko, Carbon Nanotube Reinforced Bombyx mori Silk Nanofibers by the Electrospinning Process, Biomacromolecules. 7 (2006) 208–214. https://doi.org/10.1021/bm0505888.
[30] H. Pan, Y. Zhang, Y. Hang, H. Shao, X. Hu, Y. Xu, C. Feng, Significantly Reinforced Composite Fibers Electrospun from Silk Fibroin/Carbon Nanotube Aqueous Solutions, Biomacromolecules. (2012). https://doi.org/10.1021/bm300877d.
[31] J. Wang, L. Li, M. Zhang, S. Liu, L. Jiang, Q. Shen, Directly obtaining high strength silk fiber from silkworm by feeding carbon nanotubes, Mater. Sci. Eng. C. 34 (2014) 417–421. https://doi.org/10.1016/j.msec.2013.09.041.
[32] G. Fang, Z. Zheng, J. Yao, M. Chen, Y. Tang, J. Zhong, Z. Qi, Z. Li, Z. Shao, X. Chen, Tough protein-carbon nanotube hybrid fibers comparable to natural spider silks, J. Mater. Chem. B,. 3 (2015) 3940–3947. https://doi.org/10.1039/c5tb00448a.
[33] Q. Wang, C. Wang, M. Zhang, M. Jian, Y. Zhang, Feeding Single-Walled Carbon Nanotubes or Graphene to Silkworms for Reinforced Silk Fibers, Nano Lett. 16 (2016) 6695–6700. https://doi.org/10.1021/acs.nanolett.6b03597.
[34] C. Zhang, Y. Zhang, H. Shao, X. Hu, Hybrid Silk Fibers Dry-Spun from Regenerated Silk Fibroin/Graphene Oxide Aqueous Solutions, ACS Appl. Mater. Interfaces. 8 (2016) 3349−3358. https://doi.org/10.1021/acsami.5b11245.